Remote Sensing of Environment: Accepted https://doi.org/10.1016/j.rse.2021.112499

The PRISMA imaging spectroscopy mission: overview and first performance analysis

*S. Cogliati[1] *, F. Sarti[2], L. Chiarantini[2], M. Cosi[2], R. Lorusso[3], E. Lopinto[3], F. Miglietta[4], L. Genesio[4], L. Guanter[5], A. Damm[6,7], S. Pérez-López[5], D. Scheffler[8], G. Tagliabue[1], C. Panigada[1], U. Rascher[9], T.P.F. Dowling[10], C. Giardino[11], R. Colombo[1]*

[1]Remote Sensing of Environmental Dynamics Lab., DISAT, University of Milano-Bicocca, P.zza della Scienza 1, 20126, Milano, Italy

[2]Leonardo, Via delle Officine Galileo, 1, 50013 Campi Bisenzio, Florence, Italy

[3]Italian Space Agency

[4]Institute of Bioeconomy - National Research Council - CNR-IBE, Via Caproni 8, 50145 Florence, Italy

[5]Centro de Tecnologías Físicas, Universitat Politècnica de València, Spain

[6]Department of Geography, University of Zurich, Zurich, Switzerland

[7]Eawag, Swiss Federal Institute of Aquatic Science and Technology, Dübendorf, Switzerland

[8]Helmholtz Centre Potsdam GFZ German Research Centre for Geosciences, Section Remote Sensing, Telegrafenberg, 14473 Potsdam, Germany

[9]Institute of Bio- and Geosciences, Plant Sciences (IBG-2), Forschungszentrum Jülich GmbH, 52428 Jülich, 11 Germany

[10]Department of Geography, King's College London, 40 Bush House, North East Wing, Aldwych, London WC2B 4BG

[11]Institute for Electromagnetic Sensing of the Environment, National Research Council - CNR-IREA, Via Bassini, 15 - 20133 Milano, Italy

***Corresponding author**: sergio.cogliati@unimib.it, +39-0264482913, Remote Sensing of Environmental Dynamics Lab., DISAT, University of Milano-Bicocca, P.zza della Scienza 1, 20126, Milano, Italy.

Abstract

The *PRISMA* satellite mission launched on March 22nd, 2019 is one of the latest spaceborne imaging spectroscopy mission for Earth Observation. The PRISMA satellite comprises a high-spectral resolution VNIR-SWIR imaging spectrometer and a panchromatic camera. In summer 2019, first operations during the commissioning phase were mainly devoted to acquisitions in specific areas for evaluating instrument functioning, in-flight performance, and mission data product accuracy. A field and airborne campaign was carried out over an agriculture area in Italy to collect in-situ multi-source spectroscopy measurements at different scales simultaneously with PRISMA. The spectral, radiometric and spatial performance of PRISMA Level 1 Top-Of-Atmosphere radiance (L^{TOA}) product were analyzed. The in-situ surface reflectance measurements over different landcovers were propagated to L^{TOA} using MODTRAN5 radiative transfer simulations and compared with satellite observations.

Overall, this work offers a first quantitative evaluation about the PRISMA mission performance and imaging spectroscopy L^{TOA} data product consistency. Our results show that the spectral smile is less than 5 nm, the average spectral resolution is 13 nm and 11 nm (VNIR and SWIR respectively) and it varies ± 2 nm across track. The radiometric comparison between PRISMA and field/airborne spectroscopy shows a difference lower than 5% for NIR and SWIR, whereas it is included in the 2-7% range in the VIS. The estimated instrument signal to noise ratio (SNR) is ≈ 400-500 in the NIR and part of the SWIR (< 1300 nm), lower SNR values were found at shorter (< 700 nm) and longer wavelengths (> 1600 nm). The VNIR-to-SWIR spatial co-registration error is below 8 m and the spatial resolution is 37.11 m and 38.38 m for VNIR and SWIR respectively. The results are in-line with the expectations and mission requirements and indicate that acquired images are suitable for further scientific applications. However, this first assessment is based on data from a rural area and this cannot be fully exhaustive. Further studies are needed to confirm the performance for other land cover types like snow, inland and coastal waters, deserts or urban areas.

Keywords: PRISMA, imaging spectroscopy, HyPlant, field spectroscopy, cal/val

1 Introduction

The imaging spectroscopy satellite mission *PRecursore IperSpettrale della Missione Applicativa* (PRISMA) represents an advancement in Earth Observation technology and opens new opportunities to advance hyperspectral remote sensing methods, techniques and scientific data exploitation for innovative applications. PRISMA is one of the most recent imaging spectroscopy satellites providing a follow up of National Aeronautics Space Administration's (NASA) pioneering Hyperion aboard the Earth Observing-1 satellite (EO-1) in the early 2000 (Folkman et al., 2001; Middleton et al., 2017) and decommissioned on March 30, 2017. Today, several efforts are under development by the international community and space agencies in different countries to develop and implement hyperspectral projects and space programs (Rast & Painter, 2019). These efforts rely either on dedicated orbital platforms for operational long-term mission (3-5 years) or temporary deployment on the International Space Station (ISS) for dedicated in-flight verification tests. A number of imaging spectroscopy satellites were recently launched or are in their final preparation for launch in the next few years: the Chinese Gaofen-5 Advanced Hyperspectral Imager (AHSI) (launched in May 2018), the Chinese ZY1E AHSI (launched in November 2019), the German Environmental Mapping and Analysis Program EnMAP (Guanter et al., 2015) (launch expected by mid-2022). European Space Agency's (ESA) Copernicus Hyperspectral Imaging Mission for the Environment (CHIME) (Nieke & Rast, 2018) and NASA's Surface Biology Geology (SBG) (Green, 2018; Lee et al., 2015) missions are expected after 2025. In parallel, missions like the Hyperspectral Imager for the Coastal Ocean (HICO) (Corson et al., 2008) (in operation between 2009 and 2014), the recent DLR Earth Sensing Imaging Spectrometer (DESIS) (Müller et al., 2016), the Japanese HISUI imager (Matsunaga et al., 2018) (launched in December 2019) and the USA's Earth Surface Mineral Dust Source Investigation (EMIT) (Green et al., 2020) (ready for a launch to the ISS in late 2021 and placed on ELC-1) are installed aboard the ISS (Rast & Painter, 2019).

The PRISMA mission is targeted to advance environmental remote sensing through novel and innovative approaches fostered by its unprecedented high spectral and spatial resolution across the entire visible-near infrared (VNIR) and shortwave infrared (SWIR) spectral region (Loizzo et al., 2018). Expected benefits embrace several fields of application such as topsoil property retrieval (Chabrillat et al., 2019), mapping of raw materials (Thompson et al., 2020a), forest resources and ecosystem biodiversity assessment (Gamon et al., 2019), agricultural crop monitoring (Hank et al., 2019), snow and ice surface property mapping (Bohn et al., 2020) and inland/coastal water quality assessment (Giardino et al., 2019).

The successful exploitation of imaging spectroscopy data depends on the spectral, radiometric, and spatial "quality" of the data in terms of accuracy, precision and measurement uniformity across the multi-dimensional image cube (Chapman et al., 2019; Guanter et al., 2007; Meroni et al., 2010; Thompson et al., 2018, 2019). Spectral shift, band broadening and keystone are few examples of instrumental effects that affect (degrade) the cross-track uniformity of images, with a direct negative impact on the success and reliability of scientific applications. These issues have an obvious impact when measurements are combined with Radiative Transfer (RT) models (i.e., geophysical parameter retrieval using model inversion techniques), but negatively affect even simpler image-based approaches. Instrumental effects are typically manifested and corrected at Level 1 (L1) data level, but products of higher-level processing (i.e., Level 2 products such as surface reflectance) inevitably inherit biases/uncertainties when instrumental effects are not properly corrected.

Spaceborne instruments are often characterized by dedicated on-board calibration systems including solar diffuser plates or reference lamps. These systems offer a direct way to monitor spectral and radiometric sensor drifts from the nominal pre-launch characterization/calibration. The actual center wavelength (CWL), bandwidth and radiometric response across the focal plane are systematically and routinely measured on-board during dedicated post-launch in-flight operations by means of different devices and technologies.

Alternatively, satellite cross-comparison approaches are often employed to evaluate consistency of observations collected almost simultaneously over common areas. This approach is not always optimal or possible, depending on mission orbit and the instrument's field of view specifications. Indeed, significant inter- or intra-day temporal lags can exist between observations from two satellites that can hinder a fully exhaustive quantitative analysis. This issue can be partly compensated by considering the so-called *Pseudo-Invariant Calibration Sites* (PICS) (Cosnefroy et al., 1996). However, the use of these sites has been primarily limited to satellites cross-comparison and sensor stability monitoring, with only a few attempts to develop absolute radiometric models for these sites (Helder et al., 2013). Moreover, the exploitation of desert calibration sites prevents a more comprehensive validation that ideally considers a wider variability of radiometric signatures. The recently established *Radiometric Calibration Network* (*RadCalNet*) (Bouvet et al., 2019) is an international effort to provide automated and systematic surface and atmospheric in-situ measurements to support the calibration and validation (cal/val) of remote sensing instruments. It also represents a promising approach for cal/val activities of spaceborne imaging spectroscopy missions. *RadCalNet* offers systematic field spectroscopy and atmospheric data from multiple sites according to standard protocols for collecting data, processing to Top-Of-Atmosphere (TOA) radiance (L^{TOA}), and provides uncertainty budgets traceable to the international system of units.

Other techniques were developed over the years to specifically evaluate the in-flight performance of instruments and derived products accuracy by means of vicarious and image-based methods or by comparing satellite observations with ground/airborne in-situ reference measurements. The instrument's spectral behavior is typically evaluated using spectral matching techniques that compare in-flight radiance measurements with RT model simulations in well-defined atmospheric absorption features (Guanter et al., 2007; Thompson et al., 2018). A similar approach to characterize the instrument's radiometric response is not straightforward because it largely depends on the intrinsic characteristics of the surface and atmosphere at the time of acquisition. Therefore, in-situ measurements such as *RadCalNet* are often necessary to characterize both surface reflectance and atmospheric optical properties. However, relating satellite pixels with in-situ ground sampling that typically covers limited areas (few meters) with unknown spatial variability remains challenging. Alternatively, high spatial resolution airborne imaging spectroscopy (or satellite data) can be employed during dedicated surveys to provide spatially distributed spectra and better serve satellite performance assessments.

The direct and vicarious methods briefly introduced above have their specific strengths and limitations, while a synergic combination of these different approaches would provide a more comprehensive and consolidated analysis. Although conceptually similar, ground or airborne based cal/val approaches need to be tailored for each space mission, and numerous aspects must be considered for evaluating the instruments performance and the quality of mission data products.

Based on first data resulting from the PRISMA commission phase, we aim to provide a first evaluation of the spectral, spatial and radiometric performance of PRISMA L^{TOA} imaging spectroscopy data by the end of the commissioning phase. The study is mainly conducted in a well characterized rural area in Italy, while geometric performance is assessed on a highly textured area in the US. The spectral and spatial performances were assessed by means of state-of-art vicarious and image-based techniques. The radiometric accuracy was assessed with a consistency analysis of TOA spectral radiance measured by PRISMA and modeled using in-situ ground and airborne spectroscopy measurements in a multi-scale comparison scheme.

2 The PRISMA mission and status

PRISMA is a small size satellite mission targeted at qualifying spaceborne hyperspectral technology and delivering imaging spectroscopy data to foster novel processing methods and applications for a variety of resource management and environmental monitoring applications. The satellite was built for the Italian Space Agency ASI (*Agenzia Spaziale Italiana*) by *OHB Italia Spa* as prime contractor. *Leonardo Space*

& Airborne Systems (hereafter *Leonardo*) was responsible for the payload instruments that include state-of-the-art VNIR-SWIR imaging spectrometer and a high-resolution panchromatic camera (PAN) to offer unprecedented observation capabilities (Coppo et al., 2020). The satellite was launched on March 22nd, 2019 (UTC time 01:50:35) aboard of the Vega Flight VV14 from Europe's Spaceport in Kourou, French Guiana.

PRISMA is flying on a Sun-Synchronous Low Earth Orbit at an altitude of 615 km with an inclination of 97.85º, acquisition period of 98 minutes and Local Time of equator crossing on Descending Node (LTDN) at 10:30. The expected operational mission lifetime is 5 years. The nominal orbit re-visit time is 29 days (from nadir) with a re-look capability for a specific target of 7 days with off-nadir viewing. The optical payload does not include any pointing device and off-nadir observations are performed through platform roll maneuvers (across-track or along track). The nominal geographic coverage is between 70°S - 70°N latitude (at equinoxes) and 180°W - 180°E longitude, but imagery can be acquired at higher latitudes with the only limitation related to typically low solar zenith angle (SZA). The standard size of a single image is 30 x 30 km with a Ground Sampling Distance (GSD) of 30 m (VNIR-SWIR) and 5 m (PAN), but the system can acquire full-resolution payload data up to 1800 km x 30 km (i.e., the maximum length of a single EO acquisition).

PRISMA is a pushbroom imaging spectrometer based on prism technology to obtain the dispersion of radiation on a 2-D focal plane detected by a 1000 x 256 MCT (Mercury-Cadmium-Telluride) back side illuminated pixels array to acquire several spectral bands of the same strip on the ground. The imaging spectrometer covers the nominal 400-2500 nm spectral range with two separated instruments: the VNIR spectrometer features 66 spectral bands from about 400 nm to 1010 nm, with a nominal spectral sampling interval lower than 11 nm and a bandwidth lower than 15 nm (Table 1). The SWIR detector provides 174 spectral bands between 920 to 2500 nm with a bandwidth lower than 15 nm. The two spectrometers share the same entrance telescope which is a three mirror anastigmat telescope featured by aspherical mirrors.

The panchromatic camera offers co-registered 5.1 m spatial resolution imagery useful for a better interpretation of the imaging spectrometer data. A comprehensive description of the PRISMA optical design and technical specifications for the hyperspectral imager and PAN instruments is available in Coppo et al., 2020.

The “standard” products systematically produced by the PRISMA ground processor and made available to users consist of: Level 1 TOA radiometrically and geometrically calibrated radiance images; Level 2 geolocated and geocoded atmospherically corrected images. Details can be found in the PRISMA Products Specification Document (ASI, 2020).

PRISMA has been characterized with various activities during the commissioning phase (Table 1). These activities yielded strong improvements of the mission ground processor and the data product quality from the first versions developed during the commissioning phase. The results presented in this study are based on the current version 3.6 of PRISMA products distributed to the public.

	Requirement	**VNIR**	**SWIR**	**PAN**	**V**
Swath	≥30 km	31 km	31 km	31 km	**F**
Ground Sampling Distance (GSD)	≤31 m (VNIR-SWIR) ≤5.1 m (PAN)	31 m	31 m	5.1 m	**F**
Spectral Range	400-2500 nm	400–1010 nm	920–2500 nm	400–700 nm	**-**
Number of bands	-	66	174	1	**-**
Modulation Transfer Function (MTF)	≥0.3 (VNIR-SWIR) ≥0.2 (PAN)	0.30	0.32	0.25	**F**
Spatial co-registration (GSD=30 m)	≤0.1 GSD	0.04 GSD	0.04 GSD	0.06 GSD	**F**
Spectral Sampling Interval (SSI)	≤11 nm	7.2-11 nm	6.5-11 nm	-	**G**
Spectral Resolution	≤15 nm	9-13 nm	9-14.5 nm	-	**G**

Spectral co-registration (SSI=30μm)	≤±0.1 SSI	0.08 SSI	0.05 SSI	-	**F**
SNR	≥160-200 (400-450 nm) ≥200 (450-1000 nm) (NA in absorption bands)	161-209 (400-450 nm) 200-450 (450-1000 nm)	--	--	**G**
	≥200 (1000-1750 nm) ≥100 (1950-2350 nm) (NA in absorption bands)	-	300-800 (1000-1300 nm) 200-400 (1500-1750 nm) 100-200 (1950-2350 nm)	-	**G**
	≥190 (PAN)	-	-	191	**G**
Spectral centroid knowledge Accuracy	≤±0.1 nm	±0.1 nm	±0.1 nm	-	**G**
Absolute Radiometric Accuracy	≤5%	≤5% (Stability≤±1%)	≤5% (Stability≤±1%)	-	**F**

Table 1: PRISMA technical specifications: reference mission requirements values and actual performance characterized by Leonardo Space & Airborne Systems (V column reports the Verification method: F= in-flight, G=on ground).

3 Study area and multi-source dataset

Our analysis of PRISMA imagery was mainly performed on an agricultural area in central Italy (Grosseto, 42°49'45.38"N,11°4'12.71"E), in synergy with an intensive field and airborne survey. The site is located in central Tuscany ~20 km from the coastline and consists of a patchy agricultural landscape with a variety of different crops typical for this region (i.e., corn, alfalfa, forage etc.). Several in-situ measurements were made to characterize the optical properties of different landcover types (field spectroscopy) and bulk properties of the atmosphere (sunphotometer). Parallel acquisitions with the airborne imaging spectrometer HyPlant provided spatially distributed spectral measurements over a larger area. Figure 1 shows the survey area covered by PRISMA and the location of intensive ground/airborne field spectroscopy measurements. Additionally, a PRISMA image collected on Maricopa area May 5th, 2020 (Arizona, US; 33°03'29.20" N -112°02'51.50" W), characterized by highly textured scene (Gascon et al., 2017), was additionally employed to consolidate the MTF geometric analysis. The in-situ ground/airborne and PRISMA data acquired in Italy are described in detail in the remaining part of this section.

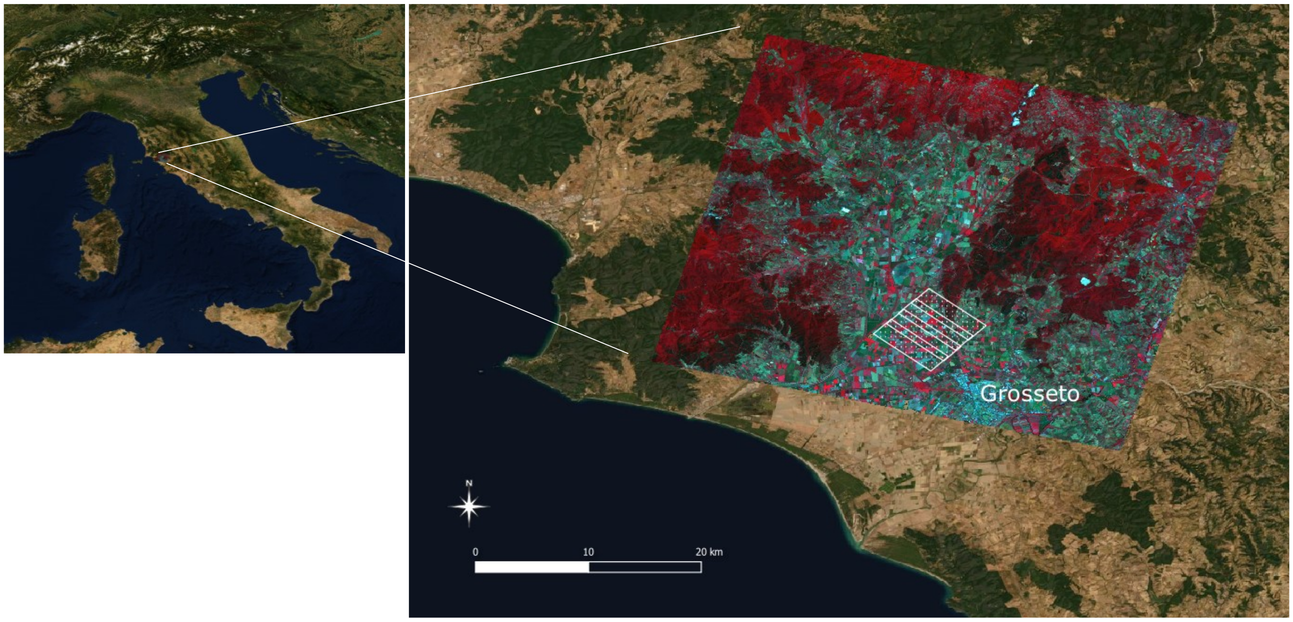

Figure 1: Geographic area covered by PRISMA imagery collected on June 16th, 2019 at 10:22 UTC over Grosseto (IT); white rectangle indicates the ground/airborne survey area.

3.1 PRISMA imagery

The PRISMA imagery was collected on June 16th, 2019 at 10:22 UTC time with a roll angle of 12° (catalog image id = 266). The overall weather conditions were stable during the entire day due to a high pressure field over the entire Mediterranean area, offering complete clear-sky conditions (PRISMA image cloud coverage 0.74%) with a relative low aerosol loads during the survey. The collected raw imagery was processed by the standard PRISMA mission ground processor (L1_A_EO) version 3.6 and the L1 imagery (PRS_L1_STD) was downloaded from the mission website (http://prisma-i.it). The PRISMA products are stored in HDF-EOS5 (Hierarchical Data Format - Earth Observing System) files and include the panchromatic, VNIR and SWIR datasets. The file also contains all information related to the platform, required instrument engineering parameters, and information necessary for the geometric processing. The original HDF-EOS5 file was converted to band sequential (BSQ) file format using a tool available in ENVI 5.5.3 (L3Harris Technologies, USA) and re-projected with a geographic lookup table (GLT) Bowtie Correction routine. The VNIR and SWIR have a spectral overlapping of few bands between 930 nm to 1034 nm, so the SWIR spectral bands are retained when VNIR and SWIR are merged into a single image file. A subset of the PAN and VNIR-SWIR imagery in different color composite representations, together with example spectra from typical vegetation, bare soil and water pond pixels is shown in Figure 2.

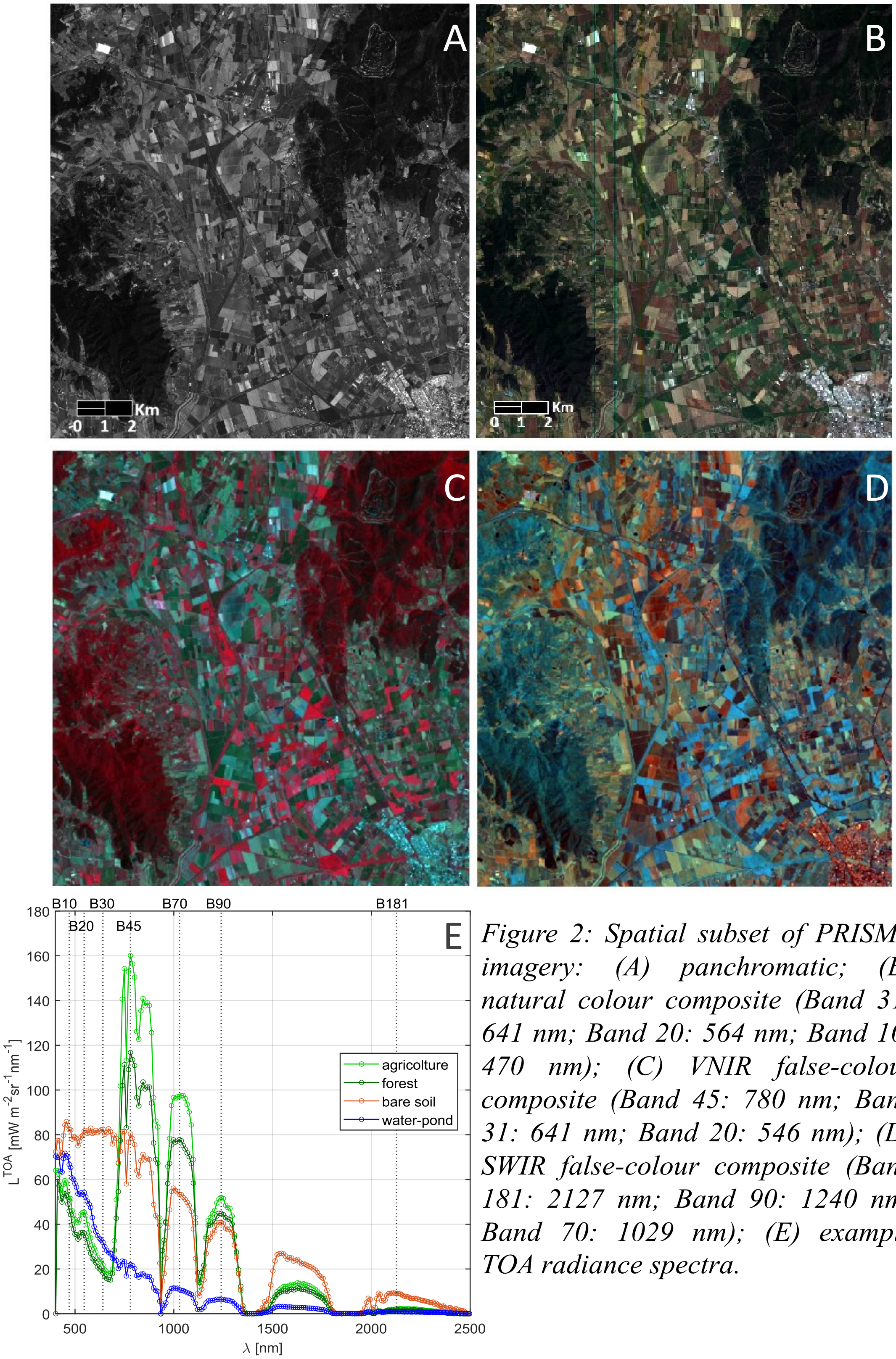

Figure 2: Spatial subset of PRISMA imagery: (A) panchromatic; (B) natural colour composite (Band 31: 641 nm; Band 20: 564 nm; Band 10: 470 nm); (C) VNIR false-colour composite (Band 45: 780 nm; Band 31: 641 nm; Band 20: 546 nm); (D) SWIR false-colour composite (Band 181: 2127 nm; Band 90: 1240 nm; Band 70: 1029 nm); (E) example TOA radiance spectra.

3.2 Airborne data

Airborne imaging spectroscopy data were collected with the HyPlant sensor (Rascher et al., 2015). HyPlant consists of two spectrometers, a very high-resolution fluorescence spectrometer (FLUO) and a traditional spectrometer (DUAL) with a spectral resolution and coverage corresponding to PRISMA. The DUAL module is a line-imaging push-broom imager, providing contiguous spectral bands from 370 to 2500 nm with an actual spectral resolution of 4 nm in the VNIR and 13 nm in the SWIR for a total of 626 spectral bands. The HyPlant SNR is about 510 in the VNIR and 1100 in the SWIR spectral regions (Rascher et al., 2015). For flight operations, the HyPlant instrument is complemented with a Data Acquisition and Power Unit and a Global Position and Inertial Navigation System (GPS/INS). The GPS/INS provides aircraft navigation data synchronous with the push-broom line scanner for image geo-referencing and rectification.

Four flight lines (L1-L4) were recorded over the experimental campaign area on June 16th, 2019 between 11:52 and 12:06 local time from a flight altitude of 3050 m, resulting in a pixel size of 4.5 m. The conversion of raw data to georeferenced calibrated at-sensor radiance was performed by the CaliGeoPro (SPECIM, Finland) software provided by the instrument manufacturer. The DUAL images were atmospherically corrected using ATCOR-4 (Richter & Schläpfer, 2002) to obtain surface reflectance. All single flight lines were mosaicked to a single image covering an area of about 5x5 km. Figure 3 shows the mosaic obtained from the four flight lines covering the test site, together with the locations of field spectroscopy sampling (section 3.3).

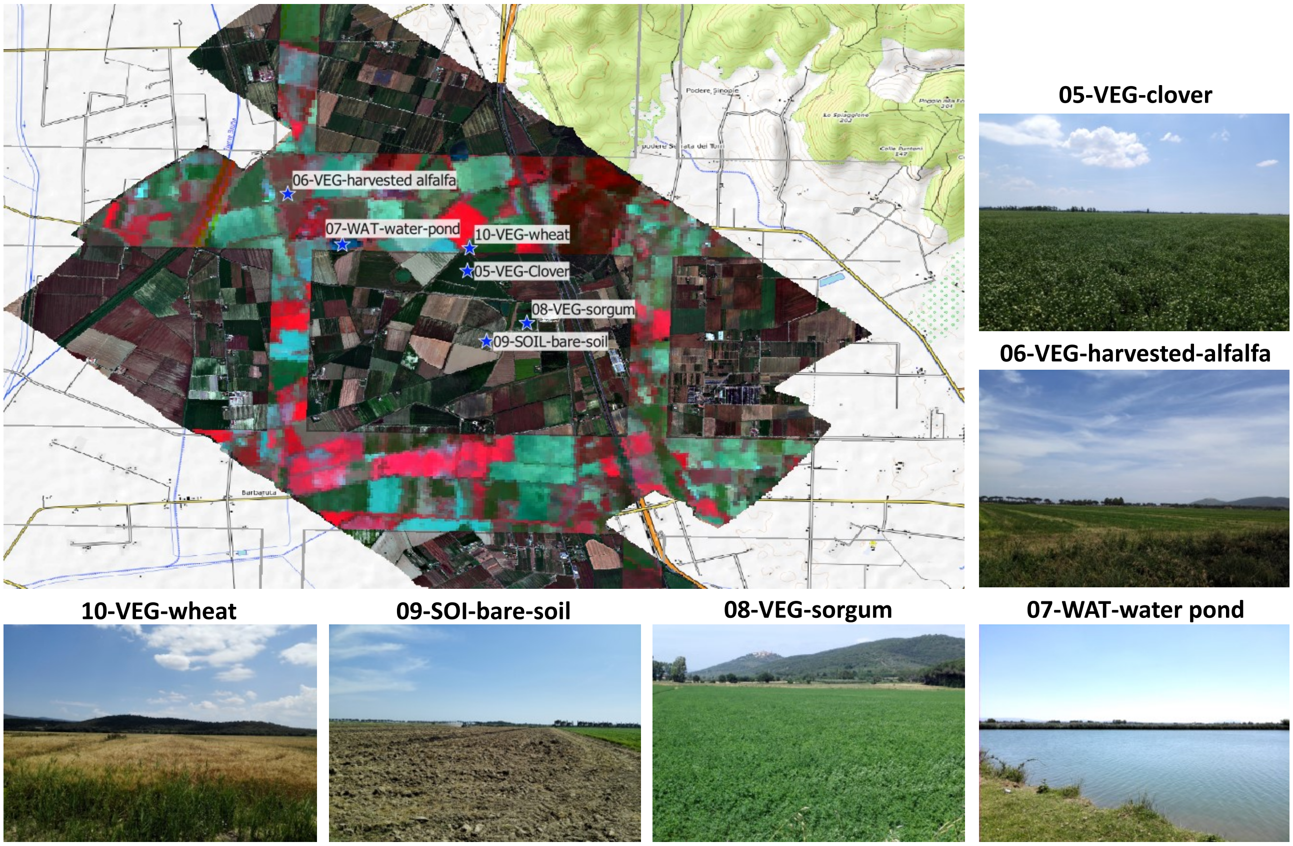

Figure 3: Blended view of PRISMA imagery (false colour composite) and HyPlant mosaic (true colour) of the study area, blue stars indicate the location of the targets measured by field spectroscopy.

3.3 Field spectroscopy and sunphotometer

Irradiance and reflected radiance of several targets in the study area were measured with the ASD FieldSpec4 (Malvern Panalytical, Longmont, CO, USA) simultaneously with PRISMA and HyPlant data acquisitions (± 1 hours). Targets were selected to capture a wide spectral variability, from bright to dark surfaces at different wavelengths. Selected targets include several crop fields, bare soil and a small water pond (Figure 3). The instrument was configured to average 10 scans before storing a single file and 20 measurements were acquired along a spatial transect to cover about 3x3 PRISMA pixels. The scheme was repeated several times on the same target. The radiance reflected by a calibrated white reference Spectralon panel was measured frequently immediately before and after each target measurement to monitor potential changes in atmospheric conditions. The conversion of the instrument raw digital numbers to calibrated radiance values was performed by the standard processing software provided by the instrument manufacturer and incorporates the latest calibration data available for the used instrument. Obtained radiance and irradiance spectra were afterwards used to calculate surface reflectance. Collected samples per PRISMA sampling site were statistically aggregated and average reflectance and standard deviation were calculated for each wavelength.

The sunphotometer measurements were collected to characterize the atmospheric status in terms of aerosol load (i.e., aerosol optical thickness at 550 nm, AOT) and columnar water vapor. The MICROTOPS II (Solar Light Company, Inc, USA) sunphotometer was operated continuously during PRISMA and airborne overpasses, sampling every 3 minutes throughout the entire survey time window. The instrument provides measurements at 440, 500, 870, 936 and 1020 nm wavelengths that are processed with the standard software provided by the instrument manufacturer. Characterized atmospheric properties are together with measured surface reflectance essential input parameters for accurate RT simulations of TOA radiances, necessary to evaluate PRISMA spectra (Section 4.2).

4 Data analysis methods

This section describes the analysis conducted to evaluate the performance of PRISMA in terms of: i) spectral characterization considering CWL and bandwidth; ii) radiometric consistency based on field and airborne in-situ data, iii) signal to noise ratio (SNR); iv) VNIR-to-SWIR spatial co-registration; and v) spatial resolution.

4.1 Spectral calibration assessment

Accurate knowledge of the spectral response of an imaging spectrometer is important for a reliable data exploitation. The spectrometers response function for each spectral band is typically represented by its

CWL, bandwidth and shape. Typically, a Gaussian function is used to model the shape of the spectral response function, with the *Full-Width at Half-Maximum* (FWHM) of the Gaussian defining the spectral resolution. The spectrometer's spectral response is usually measured during a pre-flight characterization in laboratory. In-flight methods are important to track the spectral performance during mission operations and to detect possible instrument response changes considering the nominal pre-flight characterization and during mission lifetime. Methods for in-flight spectral characterizations of imaging spectrometer using atmospheric absorption features have been developed for airborne and spaceborne instruments in the last decades. These methods rely on the comparison between measured and modelled radiance spectra in wavelength regions containing sharp spectral features caused by atmospheric absorption (Gao et al., 2004; Guanter et al., 2007; Meroni et al., 2010; Thompson et al., 2018).

In this study, high-resolution simulations of TOA radiance (L_{mod}) computed with the atmospheric RT model MODTRAN5 (Berk et al., 2006, 2011) were convolved with defined values of FWHM and CWL and compared with PRISMA Level-1 radiance spectra (L^{TOA}). The retrieval was carried out by means of non-linear optimization in which FWHM and CWL were iteratively modified until the best spectral match between simulated and observed spectrum is identified (Equation 1). The O_2 A-band at 760 nm was considered for the VNIR spectrometer, whereas the methane absorption feature at 2300 nm was investigated in the SWIR region. This process was carried out on all the image columns (cross-track) to identify variation of the CWL or FWHM across the instrument focal plane.

$$min \sum (L^{TOA} - L_{mod}(CWL, FWHM))^2 \qquad \text{Eq. 1}$$

4.2 Radiometric consistency

PRISMA radiometry was evaluated by comparing observed spectral radiance with modelled L^{TOA} spectra. L^{TOA} simulations use surface reflectance obtained from field and airborne spectroscopy in combination with the four-stream RT scheme proposed by Verhoef & Bach, 2012 and Bayat et al., 2020 and adapted to Lambertian condition:

$$L^{TOA}(\Omega_s, \Omega_v) = \frac{E_s^0 \cos(\theta_s)}{\pi}\left[\rho_{atm} + T_{dir}^{\downarrow\uparrow}\rho + \frac{T_{dif}^{\downarrow}T_{dir}^{\uparrow}\rho + (T_{dir}^{\downarrow} + T_{dif}^{\downarrow})\,T_{dif}^{\uparrow}\bar{\rho}}{1 - \bar{\rho}\,S}\right] \qquad \text{Eq. 2}$$

Ω_s and Ω_v represent the combination of zenith (θ) and azimuth (ϕ) angles for sun illumination (s) and viewing (v) angles, respectively. We neglected to indicate the dependence to all terms in Equation 2 to improve readability. The atmospheric path radiance (L_0) is computed as the product of Exo-atmospheric solar irradiance (E_s^0) corrected by the cosine of solar zenith angle and multiplied by the atmospheric bi-directional reflectance $E_s^0/\pi\ \cos(\theta)\ \rho_{atm}$. The T terms represent the different sun-to-surface ($T^{\downarrow}$) and surface-to-sensor ($T^{\uparrow}$), direct (*dir*) and diffuse (*dif*) atmospheric transmittances; S is the atmospheric spherical albedo. ρ is the pixel surface reflectance measured by field and airborne spectroscopy, while $\bar{\rho}$ represents the spatially averaged surface reflectance of the surrounding area used to compute the adjacency effect. The $\bar{\rho}$ was estimated as average value of the HyPlant mosaic, which is a reasonable assumption considering that the fragmented spatial structure of the imagery and its spectral characteristics are almost homogenous across the study area.

The atmospheric transfer functions used to propagate the surface reflectance to L^{TOA} are calculated with MODTRAN5, the aerosol optical thickness and the column water vapor derived from sunphotometer measurements were used as model input parameters. The Mid-Latitude Summer (MLS) atmospheric profile, the Thuillier et al., 2003 solar irradiance spectrum and different aerosol models (i.e., Rural, Maritime and Urban) were considered to simulate L^{TOA}. The line-of-sight parameters were defined according to the solar zenith and azimuth angles (SZA and SAA) at the time of PRISMA acquisition, the view zenith angle (VZA) was fixed according to the actual PRISMA roll angle in the image center coordinate. RT simulations were performed in high resolution in the 390-2500 nm spectral range by using a band model at 1 cm^{-1}, DISORT multiple scattering and the correlated-k options were activated to assure accurate simulations within the atmospheric absorption bands. A summary of the parameters used is reported in Table 2.

Parameter	***Unit***	***Values***
Spectral Range	nm	390 - 2500
Solar Irradiance		Thuillier et al., 2003
Molecular Band model resolution	cm^{-1}	1
Correlated-k option	-	Yes
DISORT number of streams	-	8
Atmospheric Profile	-	Mid-Latitude Summer
Aerosol Model	-	Rural, Urban, Maritime
Aerosol Optical Thickness (AOT)	-	0.12
Water vapor column	g cm^{-2}	2.3
Surface height	Km	0.02
SZA	deg	23
SAA	deg	145.8
VZA	deg	12.5

Table 2: Parameters used in MODTRAN5 atmospheric RT simulations

The atmospheric transfer functions were extracted from MODTRAN5 using the Modtran Interrogation Technique (MIT) developed by Verhoef & Bach, 2007, 2012. This technique is necessary because MODTRAN5 does not directly simulate required atmospheric transfer functions needed to simulate L^{TOA}. Different approaches have been used in past to overcome this limit. Typically, few simulations with

MODTRAN5 considering different surface albedo values are combined to calculate all functions (Guanter et al., 2009; Verhoef & Bach, 2012). The latest version of the MIT technique relies on four MODTRAN5 runs (Verhoef et al., 2018) in which different values of the surface albedo and simulations at TOA and Bottom-Of-Atmosphere are considered. In this work, the spectra obtained from this set of model runs were combined to obtain accurate estimates of the atmospheric transfer functions. Further, the so-called T-14 system introduced by Verhoef et al., 2014 for high-spectral resolution simulations in the framework of the FLEX mission (Cogliati et al., 2015 and Verhoef et al., 2018) was used to achieve an accurate modelling also within strong atmospheric absorption features. Finally, simulated L^{TOA} spectra were convolved with the PRISMA spectral response functions which were assumed gaussian (Section 4.1). An example of the atmospheric transfer functions computed is shown in supplementary material (Figure S1).

The direct comparison between ASD FieldSpec4 with PRISMA was initially performed on the sites described in Figure 3. We particularly analyzed regions of interest (ROIs) identified on the base of gps-recordings during the field sampling. For the comparison between PRISMA and HyPlant, large parts of the study area covered by airborne imagery were analyzed. The HyPlant mosaic with surface reflectance values was resampled to 30 m pixel size, regridded according to PRISMA and used in the above described RT scheme to simulate L^{TOA}. Afterward, an image segmentation algorithm available in the ENVI Feature Extraction software package (L3Harris Technologies, Inc., USA) was applied on a calculated Normalized Difference Vegetation Index (NDVI) map to systematically identify a statistically significant number of agricultural fields. This approach is particularly suitable for scenes covered by well-defined crop fields characterized by clear and sharp edges. The segmentation facilitated the comparison between PRISMA and HyPlant by automatically identifying ROIs representing pure crop fields and bare soils and excluding mixed pixels at field edges. This strategy was particularly important to minimize residuals due to spatial co-registration errors and likewise differences caused by instruments viewing angles. Obtained ROIs were further filtered to retain areas between 50.000 m^2 and 500.000 m^2 only, which correspond to medium-large size fields. In result a total of 207 ROIs distributed over the extended study area were identified, covering different landcovers (e.g. agricultural crops, forest, bare soil, surface waters). Each ROI represents a significant number of PRISMA/HyPlant pixels (45-450 pixels). Overall, simple regression techniques were employed for evaluating data consistency, but other more sophisticated techniques could be used to fully evaluate the spatial agreement (Duveiller et al., 2016).

4.3 Signal to Noise Ratio determination

Several techniques are available to assess the SNR of imaging spectroscopy data. These methods do not provide a direct quantification of instrument noise as it can be characterized in laboratory or onboard calibration systems, but give an indirect estimate of actual noise from imagery acquired in real conditions (Curran & Dungan, 1989). The general strategy is to analyze the distribution of the PRISMA L^{TOA} signal over homogeneous areas, considering the intrinsic spatial variability of natural surfaces and spectral-spatial correlation between adjacent pixels (Gao et al., 2013). More reliable methods rely on *Multiple Linear Regression* (MLR) in which inter-band (spectral) and intra-band (spatial) correlations are exploited to decorrelate the image data (Gao et al., 2013; Gao et al., 2008; Roger & Arnold, 1996). The remaining unexplained residuals are assumed to be a reliable approximation of noise. Specifically, the *Homogeneous Regions Division And Spectral De-Correlation* (HRDSDC) method (Fu et al., 2014) was used in this analysis. The method represents a noisy pixel $g(t, s, \lambda)$ at band λ and spatial location (t, s) by considering the original noise-free image signal $f(t, s, \lambda)$ and the random noise $n(f(t, s, \lambda))$:

$$g(t, s, \lambda) = f(t, s, \lambda) + n(f(t, s, \lambda)) \qquad \text{Eq. 3}$$

$\hat{g}(t,s,\lambda)$ is the predicted value for pixel $g(t,s,\lambda)$ using the MLR regression model (Equation 4) by using adjacent wavelengths $\lambda-1$ and $\lambda+1$ and neighbor pixels $g(t',s',\lambda)$ which belong to the same homogeneous region.

$$\hat{g}(t,s,\lambda) = Ag(t,s,\lambda-1) + Bg(t,s,\lambda+1) + Cg(t',s',\lambda) + D \qquad \text{Eq. 4}$$

The coefficients A, B, C and D were estimated by multiple least square regression. The residuals between predicted and actual value of the pixel can be calculated as:

$$r(t,s,\lambda) = g(t,s,\lambda) - \hat{g}(t,s,\lambda) \qquad \text{Eq. 5}$$

$r(t,s,\lambda)$ was used to obtain the noise variance calculated as sum of squared residuals and further used to compute the SNR by rationing the average signal $\mu(g(t,s,\lambda))$ and the standard deviation calculated as the squared root of the noise variance. In practice, ROIs extracted from the segmentation algorithm were used to evaluate the actual SNR of the analyzed PRISMA imagery, in particular 3x3 pixels selected in the middle of each ROIs were used in the analysis.

4.4 Spatial co-registration evaluation

Co-registration accuracy is one of the main parameters defining the spatial consistency of the data. Co-registration is defined by the vector describing the connection between the footprint of central pixels in two different spectral channels. These channels can be either consecutive (band-to-band co-registration) or located in different spectrometers (VNIR-to-SWIR co-registration). In L1 data of pushbroom spectrometers such as PRISMA, band-to-band co-registration is mostly driven by the keystone effect although structural factors and micro-vibrations also have a strong influence on the VNIR-to-SWIR co-registration. Methods for the automatic determination of band-to-band and VNIR-to-SWIR co-registration accuracy have been developed in the last years. In this study, we used the Automated and

Robust Open-Source Image Co-Registration Software (AROSICS) (Scheffler et al., 2017). In this method, tie points or brightness edges were automatically detected by applying cross-correlation techniques to the two bands under analysis.

4.5 Spatial resolution assessment

The spatial resolution of PRISMA data is related to the so-called Modulation Transfer Function (MTF), which defines the spatial frequencies captured in the data. In this study, the MTF assessment was carried out using the sharp contrast edge approach based on the implementation proposed by Choi & Helder, 2005. This method employs ground targets with a sharp contrast edge transition (Viallefont-Robinet et al., 2018). Slightly slanted targets were used to allow estimation of an oversampled Edge Spread Function (ESF) profile, obtained combining different horizontal or vertical edges. Once the ESF was obtained, its derivative was numerically calculated, providing the estimate of the instrument PSF (Point Spread Function) along the edge direction. Then, the MTF was calculated as the Fourier transform of the PSF. For estimates of the ESF, each cut of the edge target has to be centered, combined into a single array, and then interpolated to provide an ESF with sub-pixel resolution. A Fermi function was used to center each cut:

$$f(x) = \frac{a}{1 + e^{-\frac{x-b}{c}}} + d \qquad \text{Eq. 6}$$

where x represents either along-track or across-track direction, a is an amplitude parameter, b represents the center of the profile, c controls the slope of the function, and d is an offset value. Once each profile was centered, all profiles were combined into a single array and then projected onto the perpendicular axis to the edge (z-axis). The combined ESF profile was projected onto the z-axis as:

$$z = x \cos\theta \qquad \text{Eq. 7}$$

being θ the inclination angle of the edge. The inclination angle was estimated using a linear fit of the center position of each cut. A third order Savitzky-Golay filter is then used to obtain an interpolated ESF profile with sub-pixel resolution. The window width of the filter was set to 1.2 pixels, while the output resolution was set to 1/10 pixels. The LSF (Line Spread Function), representing the PSF along the edge direction, was finally calculated as the first derivative of the ESF, and then the MTF was computed as its Fourier transform:

$$MTF = \mathcal{F}_z\{LSF(z)\} \qquad \text{Eq. 8}$$

5 Results and discussion

5.1 In-flight spectral characterization

Results obtained from the spectral characterization of both, the VNIR and SWIR spectrometers are shown in Figure 4. Nominal CWL and FWHM as provided in the original PRISMA L1 file are compared to actual retrieval from in-flight data (cf. Section 4.1). Estimates for the VNIR spectrometer show a smaller peak-to-peak smile (2 nm) compared to the nominal smile (5 nm). Differences between actual and nominal smile are largest for the right side of the swath. A fluctuating pattern is also observed in CWL estimates and caused by the applied spectral resampling during the smile correction processing within the L1 processor.

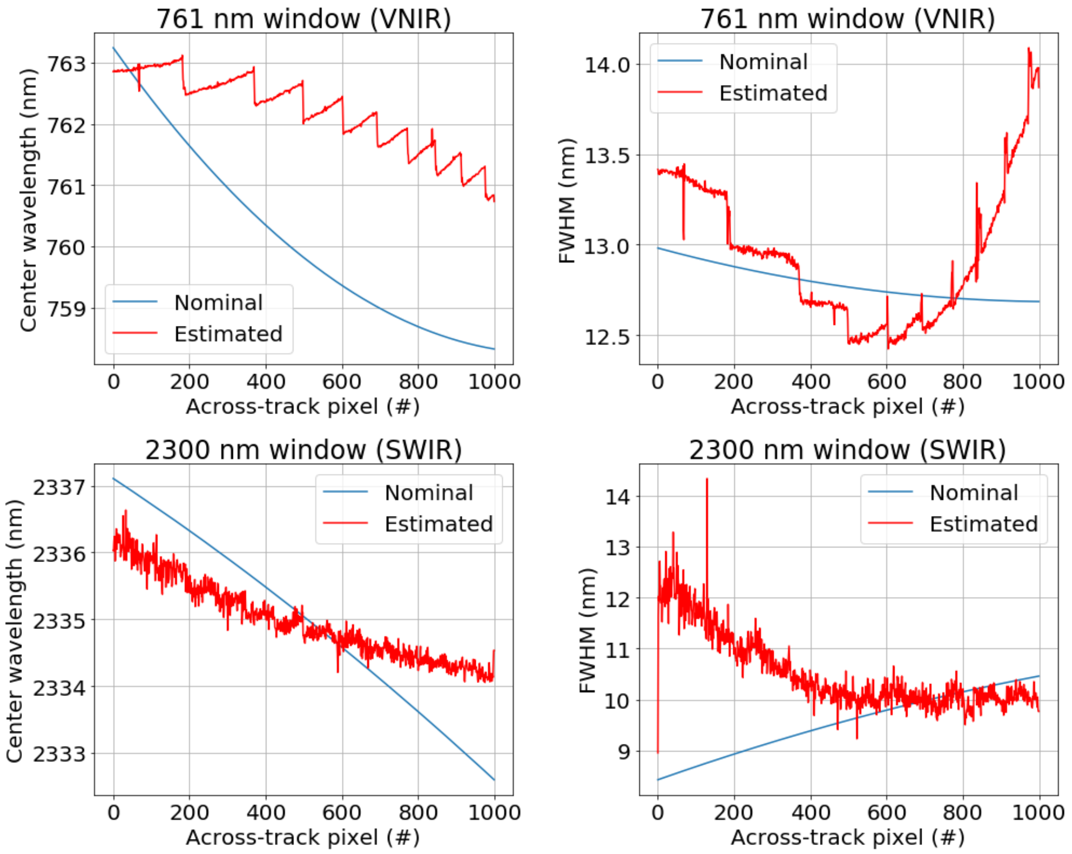

Figure 4: Nominal and estimated across-track variations in wavelength position and spectral resolution for PRISMA's VNIR and SWIR spectrometers.

The difference of estimated FWHM across track variation is less than 1.5 nm, with an average value of around 13 nm. Noticeable deviation between the nominal and actual FWHM can be observed on the right side of the swath, similar to the findings for the CWL position. For the SWIR spectrometer, nominal and estimated CWL show a better correspondence compared to the VNIR with slight underestimates of CWL on the left swath side (1 nm) and overestimates (1.5 nm) on the right side. Estimated FWHM across track variation shows a reverse pattern compared to the nominal FWHM with a largest divergence between nominal and actual FWHM on the left swath side (3.5 nm) and smallest on the right side (-0.5 nm). It must be stated that the nominal CWL and FWHM attached to the L1 images may vary from one image to another because a fine correction applied by L1 processor to account for the optical bench temperature. The results shown in Figure 4 strictly apply to the Grosseto image used in this study.

5.2 Radiometric consistency between PRISMA and field/airborne spectroscopy

Radiometric consistency was assessed by comparing measured and modelled L^{TOA}. In a first assessment, model consistency was evaluated by comparing modelled and in situ measured surface irradiance at the time of PRISMA overpass in Grosseto. The standard models of aerosol available in MODTRAN5 (Table 2) were tested to evaluate the one offering the best match. As expected, all models show a close match across the NIR-SWIR wavelength range where atmospheric scattering has a minor effect, but the urban model fits best also in the visible range. Figure S2 (supplementary material) indicates overall a close agreement between simulated and field measured irradiance, with an average relative error of 2.1% and a range between +4.7% and –10% considering absorption features. A larger discrepancy is observed for wavelengths shorter than 500 nm. However, the total error budget includes uncertainties related to both atmospheric modeling and uncertainties caused by imperfect assumptions about ASD FieldSpec4 spectral response. In fact, the high-resolution MODTRAN5 spectrum was resampled according to the nominal CWL and FWHM values of the field spectrometer from the instrument technical datasheet, whereas a more accurate characterization was not performed. This may cause larger discrepancies in spectral regions characterized by sharp absorption features.

The consistency of spectral reflectance observed by field and airborne spectrometers across landcover types investigated in the study is shown in Figure 5. The comparison is performed directly on simulated L^{TOA} because the same atmospheric transfer functions are applied to both data sets and the resulting spectra have a consistent spectral sampling (PRISMA bands). The scatterplots between ground and airborne data refer to the average and standard deviation for each wavelength obtained from aggregated field measurements and from the statistical analysis of ROIs extracted from the HyPlant imagery for each individual target (Figure 5). The spectral signatures are highly correlated with R^2 values above 0.99, the slopes of the linear regression models are close to one and offsets are almost zero. The root mean square error (RMSE) is always lower than 3.1 mW/m^2/sr/nm for all targets. The statistics indicate a good agreement for most of the selected agricultural fields and bare soils sites. Larger errors are observed for the water pond due to the small surface size and bottom influence, in particular the latter effect is probably accentuated because in-situ measurements were collected with a tilted viewing angle from shore.

In general, it is important to understand that reflectance from field and airborne spectrometers are obtained with two completely different approaches. Down-welling irradiance and up-welling radiance measured by a field spectrometer are directly converted to surface reflectance and thus exclude any potential data processing bias. Conversely, hyperspectral airborne images require an atmospheric correction to convert at-sensor radiance to surface reflectance, a step which can introduce biases in the retrieved spectra depending on the actual atmospheric conditions.

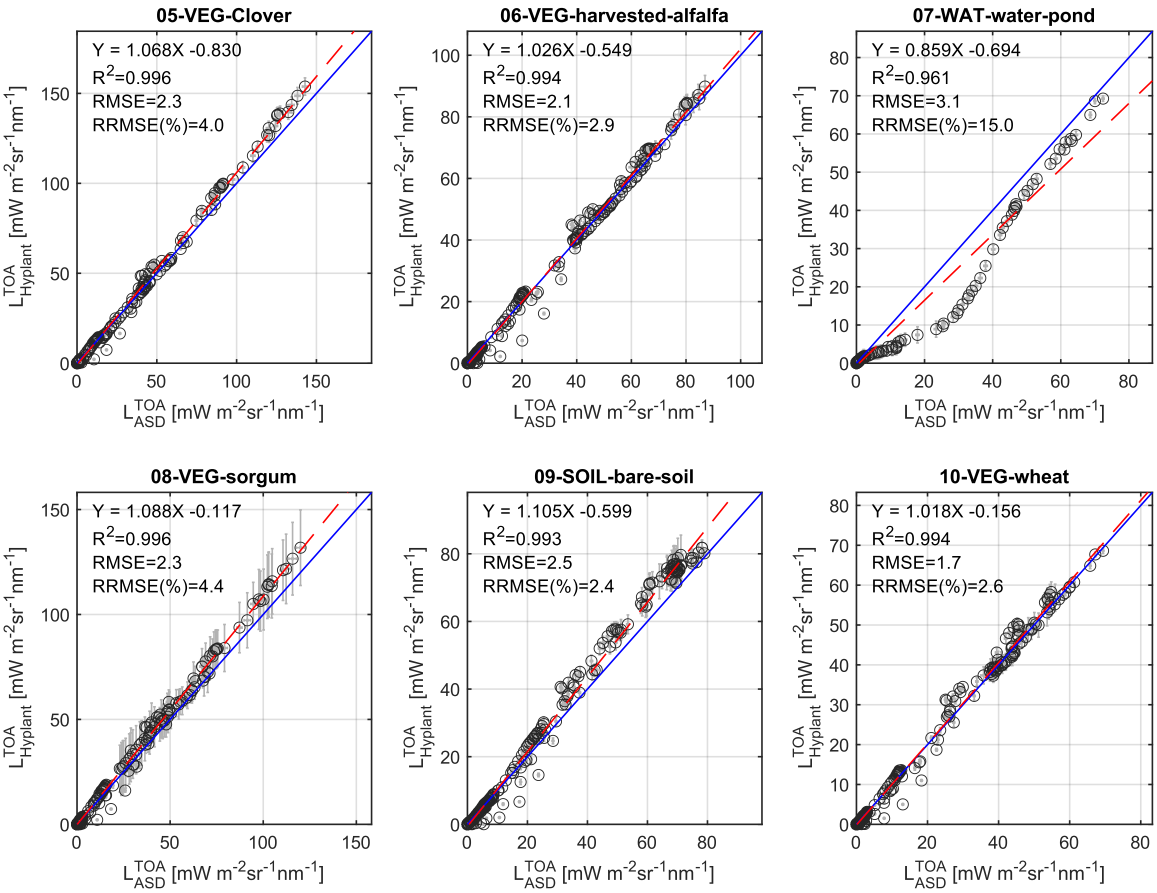

Figure 5: Scatterplot between field and airborne spectroscopy measurements over selected sites. Error bars represent the standard deviation of the ROIs extracted from the HyPlant imagery and from field measurements. The blue line is the 1:1, the red line is the least square linear model.

L^{TOA} spectra simulated from ground/airborne surface reflectance and PRISMA L1 observations are compared in Figure 6. The spectra obtained across different scales are generally consistent for all land cover types. L^{TOA} at the different wavelengths are very similar and PRISMA spectra are almost always within the standard deviation of the field/airborne measurements or within their differences.

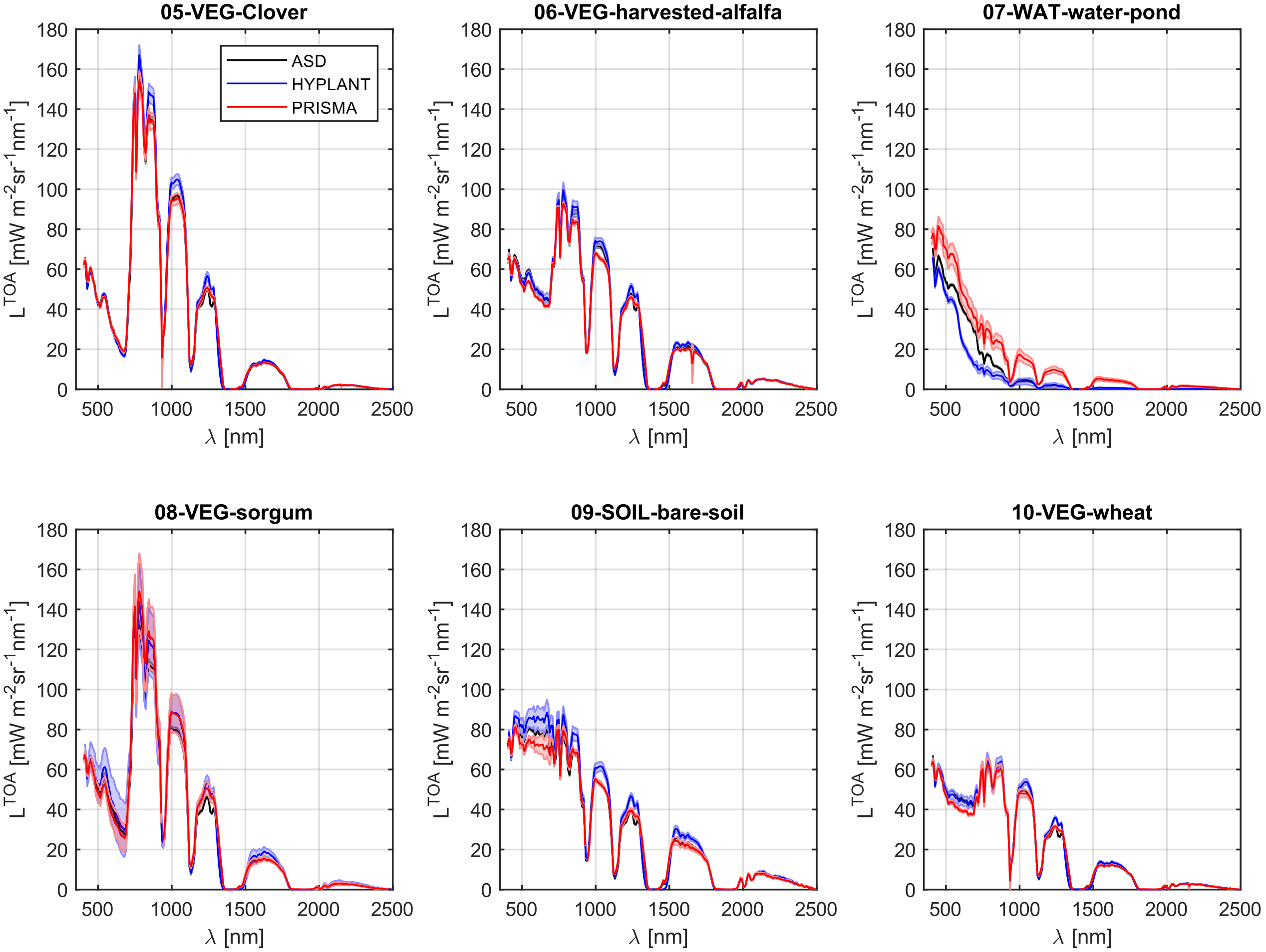

Figure 6: TOA radiance spectra observed by PRISMA (red dots) vs. TOA spectra predicted by using field (gray) and airborne (blue) spectroscopy for different targets.

The consistency of PRISMA and in-situ field spectroscopy has been further quantified in Figure 7 in terms of relative mean absolute difference per spectral band (Botchkarev, 2018). The water pond was removed from the analysis because of the difficulty in matching in-situ and PRISMA observations on this specific target. In general, the difference is always lower than 10% (excluding few SWIR wavelengths). Particularly, the VIS shows differences between 2-7%, the NIR and SWIR has differences lower than 5%, and error slightly rises up for few wavelengths larger than 2300 nm. The different viewing angles among in-situ and satellites data can cause the subtle difference observed in the green and red, however these wavelengths are typically more affected by canopy anisotropy and soil background in case of fractional vegetation cover below 100%. Absorption features were removed from the comparison since the signal is very low and even small errors in modeling L^{TOA} and instrument spectra response function might produce larger errors. Errors in absorption features originate either from small uncertainties in assumptions on the instrument spectral response function or from small errors in the atmospheric radiative transfer modelling within these regions. Therefore, further analysis should be conducted in this context also considering the atmospheric absorption features and a per-pixel retrieval of the atmospheric water vapor.

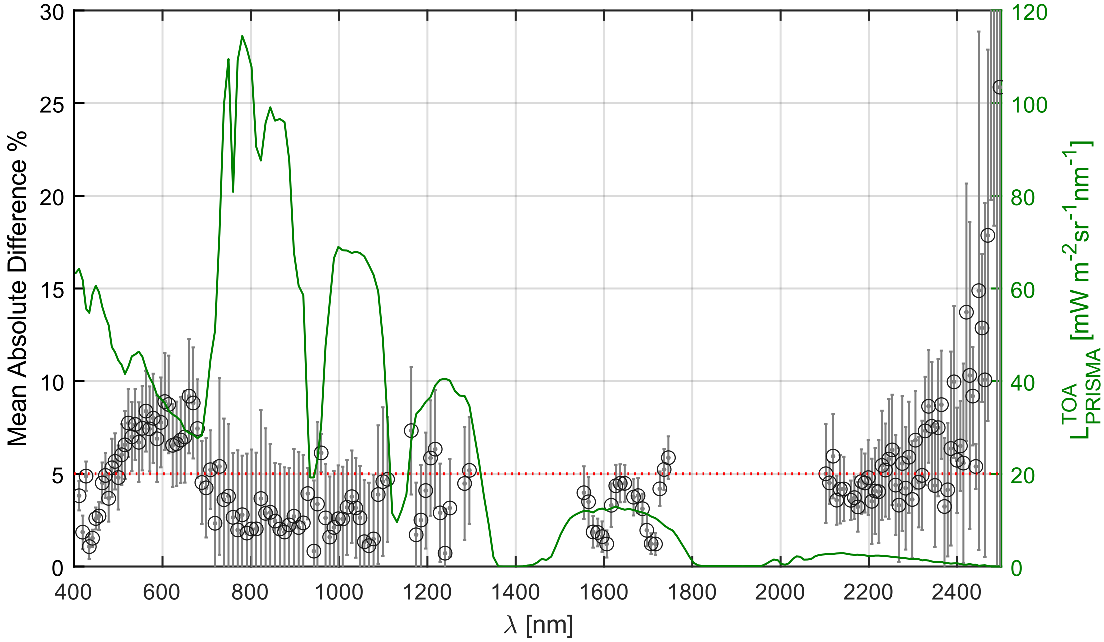

Figure 7: Relative mean absolute difference (circles) and standard deviation (vertical bars) calculated over the six targets between PRISMA L1 and TOA radiance predicted from ASD FieldSpec4 at different wavelengths; dotted red line indicates 5% difference threshold; green line is a typical vegetation spectrum observed by PRISMA.

The strong advantage of airborne imaging spectroscopy is to offer systematic and spatially distributed measurements over the entire area of interest that can be better compared with satellite data. The spatial comparison between PRISMA and L^{TOA} simulated from HyPlant is based on the analysis of the large number of ROIs identified in the study area. A number of spectral bands were selected outside the main atmospheric absorption features and the average and standard deviation values are depicted in Figure 8. A robust relationship is observed for all wavelengths $R^2 > 0.95$ considering the different level of radiance from the analyzed landcover types (i.e., bare soils, diverse vegetation types). The slope of the linear least square models is generally higher than 0.82, the RMSE values are in the range of $1.6 - 3.0\ mW\ m^{-2} sr^{-1} nm^{-1}$ in the visible; between $2.8 - 3.1\ mW\ m^{-2} sr^{-1} nm^{-1}$ in the near-infrared and lower of $2.7\ mW\ m^{-2} sr^{-1} nm^{-1}$ in the short wave infrared.

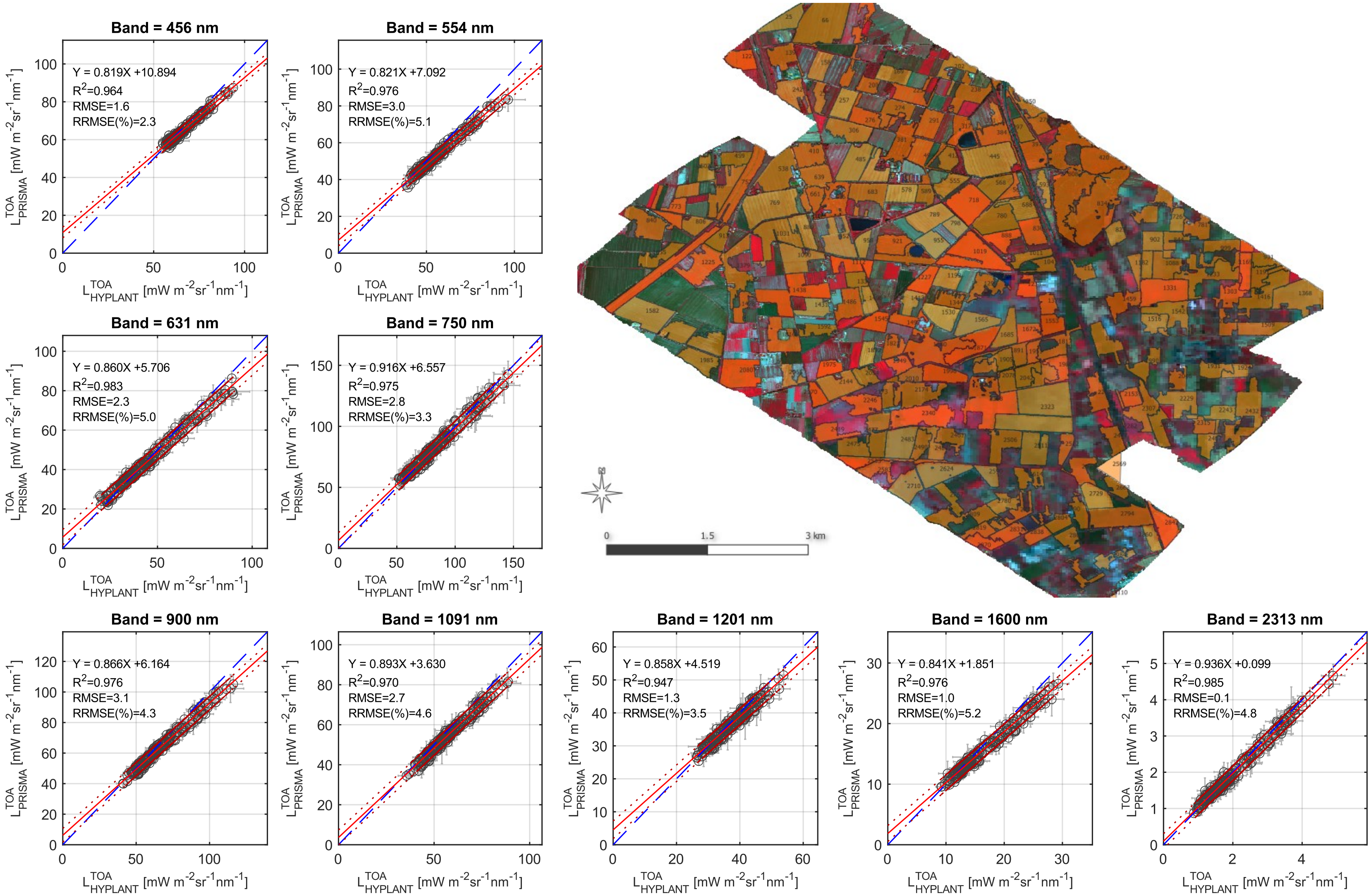

Figure 8: Comparison of TOA radiance predicted from HyPlant and PRISMA observations for selected spectral bands. Scatterplots at different wavelengths refers to average and standard deviation values of the several ROIs (n = 207) obtained from the segmentation (ROIs are overlaid to the airborne mosaic). The blue dashed line is the 1:1; red line is the linear least square model and red dotted line represent the confidence interval.

The relative mean absolute difference of L^{TOA} calculated for individual PRISMA spectral bands are shown in Figure 9. In general, the VIS spectral region is characterized by a relative difference equal or lower than 5%, with the tendency to slightly decrease toward NIR to values lower of 5%. The relative difference slightly increases in the SWIR to values of around 5-7% and it only exceeds 10% for few SWIR wavelengths at the far limit of the spectrum. Figure 9 reveals a generally good agreement between airborne and satellite L^{TOA}. This finding is consistent with previous results obtained from field spectroscopy (Figure 7). However, observed values are in average in the range of typical uncertainty values 2-5% reported in literature from a number of similar studies in which in-situ and remote sensing observations were compared (Richter & Schläpfer, 2002; Thompson et al., 2015; Thompson, Guanter, et al., 2019).

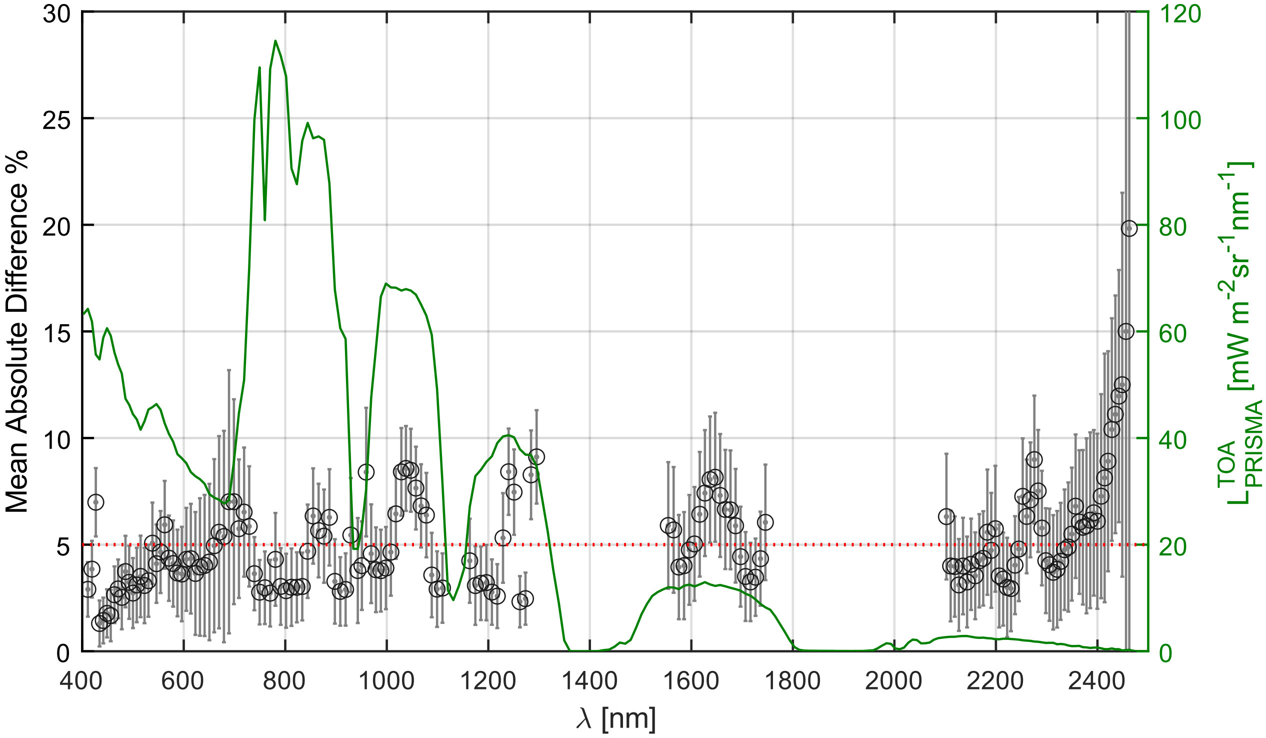

Figure 9: Relative mean absolute difference (circles) and standard deviation (vertical bars) between PRISMA L1 and TOA radiance predicted from HyPlant ROIs (n = 207); dotted red line indicates 5% difference threshold; green line is a typical vegetation spectrum observed by PRISMA.

5.3 Signal-to-noise

PRISMA's SNR estimated from L1 product using hundreds of ROIs obtained from image segmentation is presented in Figure 10. Gray dotted lines represent the spectral SNR estimated over the individual ROIs. The observed SNR variability is intrinsically affected by the target brightness and heterogeneity which complicate the characterization of SNR: bright areas characterized by a more ideal homogeneous behavior have larger SNR, conversely darker and more heterogeneous targets have a lower SNR. The 90-98% percentiles range (blue lines) is also shown to defocus from the natural variability observed in real scenes and represents the “peak” SNR values. Conceptually these values are more indicative about the instrument’s SNR as characterized in laboratory.

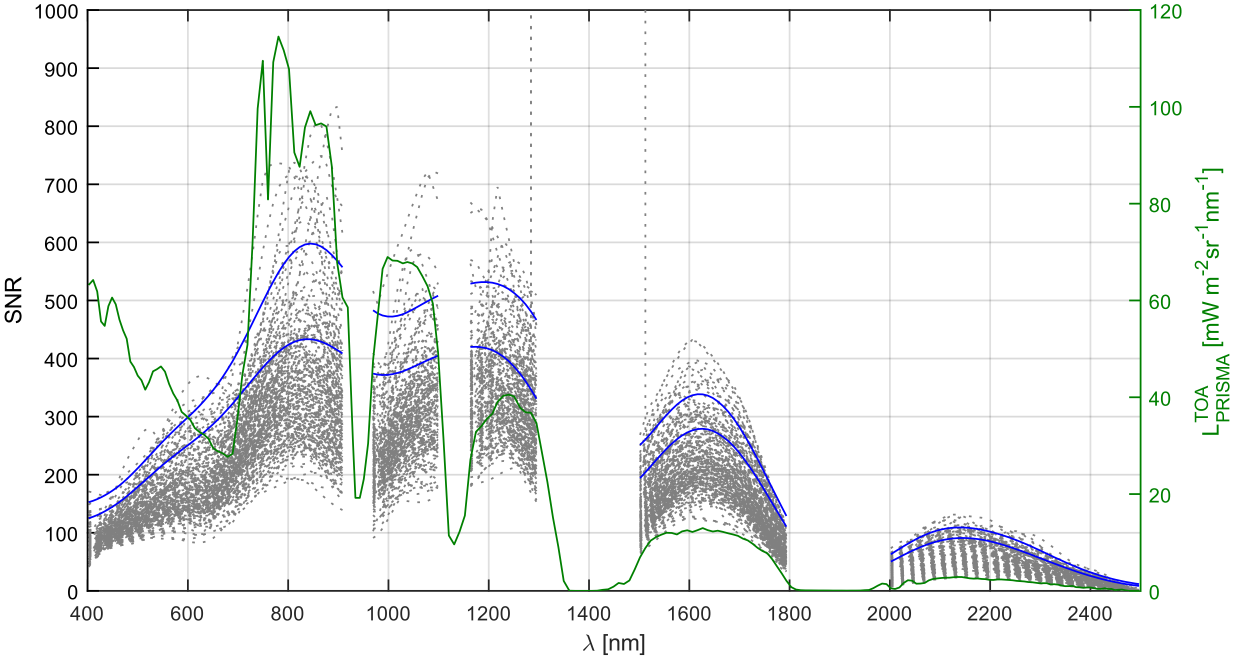

Figure 10: Per-band Signal-to-Noise Ratio estimated over 207 targets by considering 3x3 blocks (light gray dotted lines); blue lines are 90-98% percentiles; green line is a reference PRISMA TOA radiance spectrum.

The “peak” noise estimated from the real imagery shows a rising trend from SNR ≈ 200 to ≈ 400 from green to far-red wavelengths (500-700 nm). Slightly lower values were observed in the blue region and might be caused by the lower efficiency of PRISMA optical system (MCT detector) at the edge of the observed VIS spectrum. In the NIR, the SNR is between ≈ 400-500 and similar values were observed in the first part of the SWIR (up to 1300 nm). Lower SNR ≈250-300 was found around 1600 nm and SNR of ≈100 at wavelengths larger than 2000 nm. The estimated values at different wavelengths nearly agree with pre-launch characterization measurements performed by *Leonardo* (Coppo et al., 2020).

5.4 Spatial co-registration

Results from the VNIR-to-SWIR spatial co-registration analysis are summarized in Figure 11 and represent the x and y components of spatial shifts between the VNIR and SWIR spectrometers (band 64 and 73, respectively). Results show that the absolute values of the spatial shifts are typically below 8 m, with shifts in the x direction being substantially larger than those in the y direction. It must be stated that these shifts correspond to L1 data, to which a spatial alignment operation in the x-direction has been applied. Spatial shifts >1 spatial pixel (30 m) are present in the original L0 data since there is a temporal shift in the acquisition of data by each spectrometer.

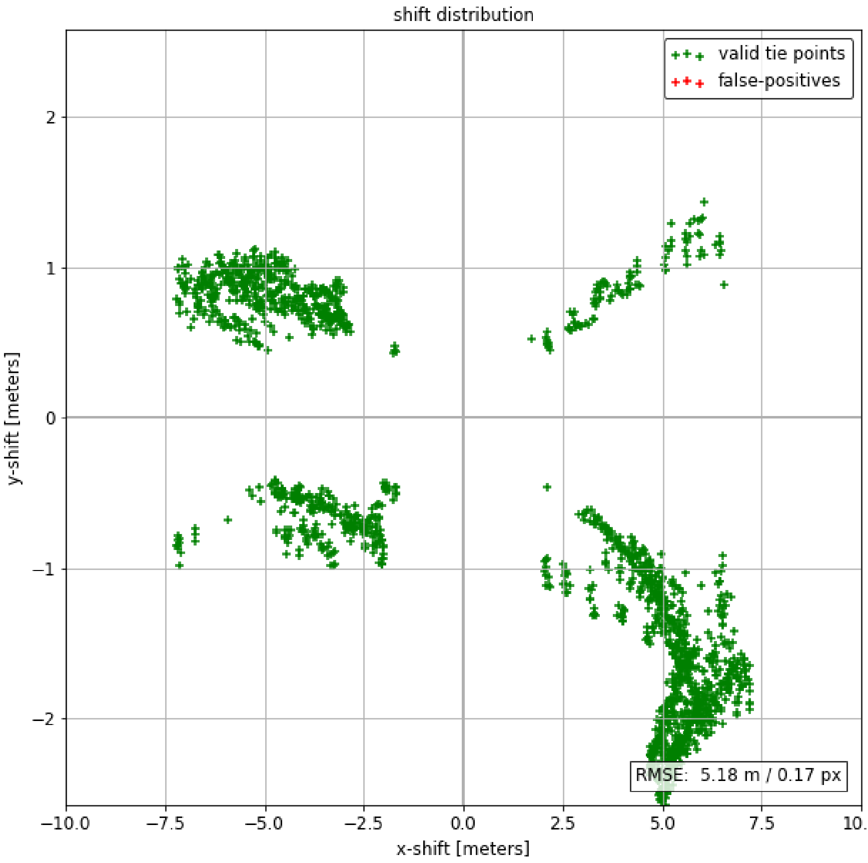

Figure 11: Spatial shifts between PRISMA's channel 64 (VNIR spectrometer) and channel 74 (SWIR spectrometer) in the across- and along-track directions estimated by AROSICS

5.5 Spatial resolution

Crop fields from Maricopa (Arizona, USA) were used to perform a preliminary along-track MTF and PSF estimate. Results were computed for those VNIR and SWIR bands in which the contrast between the low level and the high level of the ESF is enough to provide a good estimate. At least 30 spectral bands have been analyzed for each instrument to obtain the results. Figure 12 depicts estimated spatial FWHM and MTF values at Nyquist frequency as a function of band number for both VNIR and SWIR instruments. As can be observed from the figure, the PSF and MTF assessment has been performed for bands 1 to 34 of the VNIR instrument. The spatial FWHM is calculated from the LSF estimate and represents the spatial resolution of the instrument along the edge direction.

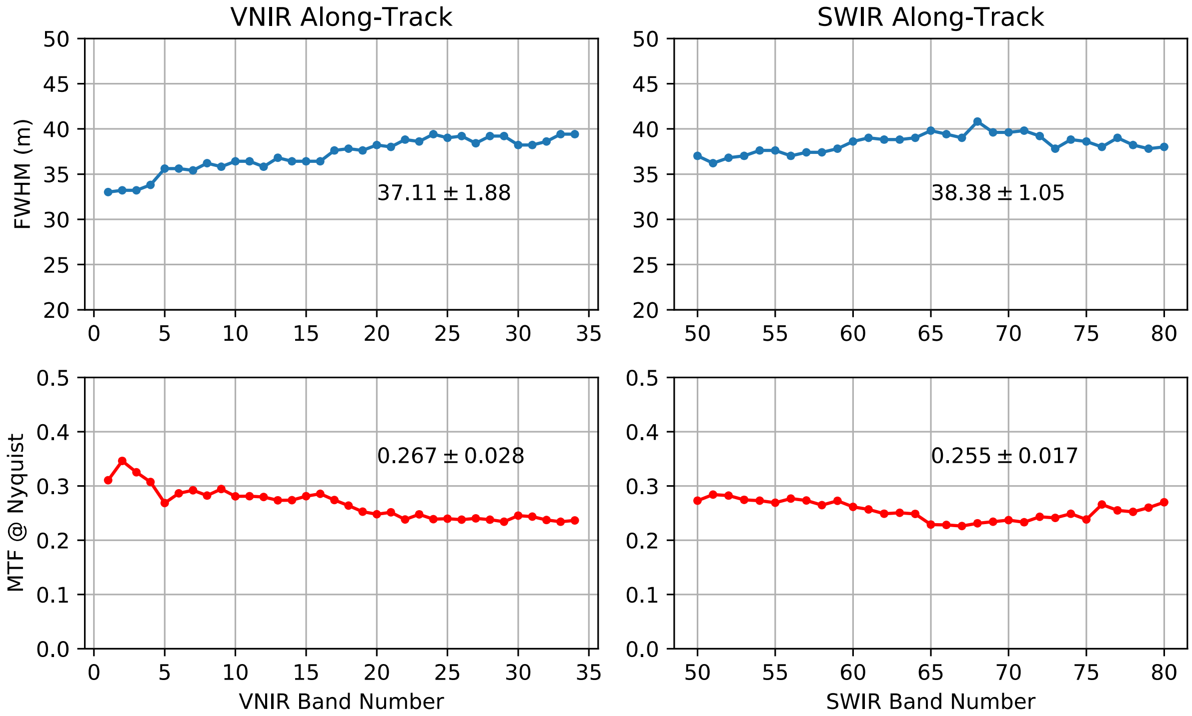

Figure 12: Along-Track results: FWHM resolution (top) and MTF at Nyquist frequency (bottom) as a function of the band number. VNIR instrument (left) and SWIR (right).

The results show that the instrument achieves a mean resolution of spatial FWHM ≈ 37.11 m, which in terms of the GSD represents about 1.24 GSD. The standard deviation of the series is $\sigma_{FWHM} \approx 1.88$ m (0.063GSD). The MTF values for the VNIR instrument are given for the spatial Nyquist frequency, that is, $f_x = 1/(2\text{GSD})$. In this case, the mean MTF value at Nyquist is $\text{MTF}^{\text{nyq}} \approx 0.267$, with a standard deviation of $\sigma_{MTF^{nyq}} \approx 0.028$. In the case of the SWIR instrument, estimates have been performed for band 50 to 80. As shown in Figure 12, the SWIR instrument provides a mean FWHM ≈ 38.38 m (1.28GSD), with a standard deviation of $\sigma_{FWHM} \approx 1.05$ m (0.035GSD). For MTF, the SWIR instrument achieves a mean MTF value at Nyquist of $\text{MTF}^{\text{nyq}} \approx 0.255$ and a standard deviation of $\sigma_{MTF^{nyq}} \approx 0.017$.

Therefore, both VNIR and SWIR instruments meet the MTF along-track requirements as shown in Table 1.

6 Conclusions

The PRISMA mission is successfully operating after its launch and is currently collecting data all over the globe. Different analyses have been conducted in this study to evaluate the quality of the Level 1 Top-Of-Atmosphere imaging spectroscopy data. We evaluated key parameters related to the spectral, spatial and radiometric performance of PRISMA. The spectral matching technique was applied on VNIR and SWIR radiance spectra to characterize CWL and FWHM, while PRISMA radiometry was evaluated by comparing observed spectral radiance with TOA spectra simulated propagating surface reflectance estimated by field and airborne spectroscopy. The co-registration of VNIR-to-SWIR spectrometers and MTF have been evaluated with image-based state-of-art algorithms. Overall, the results so far are highly promising and in-line with the expectations and mission requirements, the acquired images are suitable for use in scientific applications.

The presented analysis is mainly based on one PRISMA scene. This cannot be exhaustive and further studies are needed to confirm our results and extend performance analysis to other landcover types like snow, inland and coastal waters, deserts or urban areas. For example, a similar study dedicated to inland and coastal waters was recently developed (Giardino et al., 2020), with findings closely related to those obtained in this study. Additional analysis based on different approaches such as the analysis of data collected on PICS and Lunar calibration would be useful to further consolidate the current findings. This work does not claim to provide re-calibration coefficients for the PRISMA mission. Instead, it offers an analytical framework and first quantitative insight about the mission performance and data product quality for a typical rural area in the Mediterranean region during summer. Our outcomes will foster further exploitations of PRISMA for advancing image processing methods and innovative image spectroscopy applications.

This work analyzed L1 product only since it is the base for subsequent data products and due to the main focus of the commissioning phase on instrument performance and data processing at L0 and L1. The L1 product is mainly of interest for experienced users to exploit the potential of coupled surface-atmosphere retrievals or their own atmospheric correction (Thompson et al., 2020b; Thompson et al., 2019). However, surface reflectance (L2 product) is regularly processed and made available from ASI, but further studies are needed to assess in detail the quality of this data product level.

We conclude that based on preliminary data and this first performance assessment, it is reasonable to affirm that PRISMA represents an important step forward in the field of satellite imaging spectroscopy. The availability of PRISMA products will significantly contribute to applications and research to tackle societal and environmental challenges facing humanity.

Acknowledgments

This work was made possible by the funding support of the agreement ASI-CNR, n. 20195HH0 “Attività scientifica di CAL/VAL della missione PRISMA - PRISCAV”. The airborne-ground campaign was supported by the FLEXSense 2019 (CCN1) campaign founded by the European Space Agency. We are grateful with L3Harris Technologies (Italy) to have made available PRISMA reader integrated in ENVI in its early implementation stage. We also thanks Giulio Borgia owner of Azienda Agricola Le Rogaie for hosting the field experiments.

References

(ASI), A. S. I. (2020). *PRISMA Products Specification Document Issue 2.1 Date 12/02/2020*.

Bayat, B., van der Tol, C., & Verhoef, W. (2020). Retrieval of land surface properties from an annual time series of Landsat TOA radiances during a drought episode using coupled radiative transfer models. *Remote Sensing of Environment*, *238*, 110917. doi:10.1016/j.rse.2018.09.030

Berk, A., Anderson, G. P., Acharya, P. K., Bernstein, L. S., Muratov, L., Lee, J., … Shettle, E. P. (2006). MODTRAN5: 2006 update. In *Proceedings of SPIE - The International Society for Optical Engineering* (Vol. 6233 II). Retrieved from http://www.scopus.com/inward/record.url?eid=2-s2.0-33748645760&partnerID=40&md5=e8bf5b2b7e689457d4bd5d4efd941a4c

Berk, A., Anderson, G. P., Acharya, P. K., & Shettle, E. P. (2011). MODTRAN 5.2.1 User's Manual. Spectral Sciences, Inc., 4 Fourth Ave., Burlington, MA 01803-3304, Air Force Research Laboratory, Space Vehicles Directorate, Air Force Materiel Command, Hanscom AFB, MA 01731-3010.

Bohn, N., Guanter, L., Kuester, T., Preusker, R., & Segl, K. (2020). Coupled retrieval of the three phases of water from spaceborne imaging spectroscopy measurements. *Remote Sensing of Environment*, *242*, 111708. doi:10.1016/j.rse.2020.111708

Botchkarev, A. (2018). Performance Metrics (Error Measures) in Machine Learning Regression, Forecasting and Prognostics: Properties and Typology. *Interdisciplinary Journal of Information, Knowledge, and Management*, *14*, 45–76. doi:10.28945/4184

Bouvet, M., Thome, K., Berthelot, B., Bialek, A., Czapla-Myers, J., Fox, N., … Woolliams, E. (2019). RadCalNet: A Radiometric Calibration Network for Earth Observing Imagers Operating in the Visible to Shortwave Infrared Spectral Range. *Remote Sensing*, *11*(20), 2401. doi:10.3390/rs11202401

Chabrillat, S., Ben-Dor, E., Cierniewski, J., Gomez, C., Schmid, T., & van Wesemael, B. (2019, May 1). Imaging Spectroscopy for Soil Mapping and Monitoring. *Surveys in Geophysics*. Springer Netherlands. doi:10.1007/s10712-019-09524-0

Chapman, J. W., Thompson, D. R., Helmlinger, M. C., Bue, B. D., Green, R. O., Eastwood, M. L., … Lundeen, S. R. (2019). Spectral and Radiometric Calibration of the Next Generation Airborne Visible Infrared Spectrometer (AVIRIS-NG). *Remote Sensing*, *11*(18), 2129. doi:10.3390/rs11182129

Choi, T. ., & Helder, D. L. . (2005). Generic Sensor Modeling For Modulation Transfer Function (MTF) Estimation. In *Proceedings of the Pecora 16 Global Priorities in Land Remote Sensing, Sioux Falls, South Dakota, USA, 23–27 October 2005.*

Cogliati, S., Verhoef, W., Kraft, S., Sabater, N., Alonso, L., Vicent, J., … Colombo, R. (2015). Retrieval of sun-induced fluorescence using advanced spectral fitting methods. *Remote Sensing of Environment*, *169*, 344–357. doi:10.1016/j.rse.2015.08.022

Coppo, P., Brandani, F., Faraci, M., Sarti, F., Dami, M., Chiarantini, L., … Cosi, M. (2020). Leonardo Spaceborne Infrared Payloads forEarth Observation: SLSTRs for CopernicusSentinel 3 and PRISMA Hyperspectral Camera forPRISMA Satellite. *Applied Optics*. doi:10.1364/AO.389485

Corson, M. R., Korwan, D. R., Lucke, R. L., Snyder, W. A., & Davis, C. O. (2008). The hyperspectral imager for the coastal ocean (HICO) on the international space station. In *International Geoscience and Remote Sensing Symposium (IGARSS)* (Vol. 4). doi:10.1109/IGARSS.2008.4779666

Cosnefroy, H., Leroy, M., & Briottet, X. (1996). Selection and characterization of Saharan and Arabian desert sites forthe calibration of optical satellite sensors. *Remote Sensing of Environment*, *58*(1), 101–114. doi:10.1016/0034-4257(95)00211-1

Curran, P. J., & Dungan, J. L. (1989). Estimation of signal-to-noise: A new procedure applied to AVIRIS data. *IEEE Transactions on Geoscience and Remote Sensing*, *27*(5), 620–628. doi:10.1109/TGRS.1989.35945

Duveiller, G., Fasbender, D., & Meroni, M. (2016). Revisiting the concept of a symmetric index of agreement for continuous datasets. *Scientific Reports*, *6*(1), 1–14. doi:10.1038/srep19401

Folkman, M. A., Pearlman, J., Liao, L. B., & Jarecke, P. J. (2001). EO-1/Hyperion hyperspectral imager design, development, characterization, and calibration</title> In W. L. Smith & Y. Yasuoka (Eds.), *Hyperspectral Remote Sensing of the Land and Atmosphere* (Vol. 4151, pp. 40–51). SPIE. doi:10.1117/12.417022

Fu, P., Li, C., Xia, Y., Ji, Z., Sun, Q., Cai, W., & Feng, D. D. (2014). Adaptive noise estimation from highly textured hyperspectral images. *Applied Optics*, *53*(30), 7059. doi:10.1364/ao.53.007059

Gamon, J. A., Somers, B., Malenovský, Z., Middleton, E. M., Rascher, U., & Schaepman, M. E. (2019, May 1). Assessing Vegetation Function with Imaging Spectroscopy. *Surveys in Geophysics*. Springer Netherlands. doi:10.1007/s10712-019-09511-5

Gao, B.-C., Montes, M. J., & Davis, C. O. (2004). Refinement of wavelength calibrations of hyperspectral imaging data using a spectrum-matching technique. *Remote Sensing of Environment*, *90*(4), 424–433. doi:http://dx.doi.org/10.1016/j.rse.2003.09.002

Gao, L., Du, Q., Zhang, B., Yang, W., & Wu, Y. (2013). A comparative study on linear regression-based noise estimation for hyperspectral imagery. *IEEE Journal of Selected Topics in Applied Earth Observations and Remote Sensing*, *6*(2), 488–498. doi:10.1109/JSTARS.2012.2227245

Gao, L. R., Zhang, B., Zhang, X., Zhang, W. J., & Tong, Q. X. (2008). A new operational method for estimating noise in hyperspectral images. *IEEE Geoscience and Remote Sensing Letters*, *5*(1), 83–87. doi:10.1109/LGRS.2007.909927

Gascon, F., Bouzinac, C., Thépaut, O., Jung, M., Francesconi, B., Louis, J., … Fernandez, V. (2017). Copernicus Sentinel-2A Calibration and Products Validation Status. *Remote Sensing*, *9*(6), 584. doi:10.3390/rs9060584

Giardino, C., Brando, V. E., Gege, P., Pinnel, N., Hochberg, E., Knaeps, E., … Dekker, A. (2019, May 1). Imaging Spectrometry of Inland and Coastal Waters: State of the Art, Achievements and Perspectives. *Surveys in Geophysics*. Springer Netherlands. doi:10.1007/s10712-018-9476-0

Giardino, C., Bresciani, M., Braga, F., Fabretto, A., Ghirardi, N., Pepe, M., … Colmbo, R. (2020). First evaluation of PRISMA Level 1 data for water applications. *Sensors*, *(SUBMITTED*.

Green, R. O. (2018). Global VSWIR imaging spectroscopy and the 2017 decadal survey: Robert O. Green and the imaging spectroscopy community. In *International Geoscience and Remote Sensing Symposium (IGARSS)* (Vol. 2018-July, pp. 183–185). Institute of Electrical and Electronics Engineers Inc. doi:10.1109/IGARSS.2018.8518744

Green, R. O., Mahowald, N., Ung, C., Thompson, D. R., Bator, L., Bennet, M., … Zan, J. (2020). The Earth Surface Mineral Dust Source Investigation: An Earth Science Imaging Spectroscopy Mission. In *IEEE Aerospace Conference Proceedings*. IEEE Computer Society. doi:10.1109/AERO47225.2020.9172731

Guanter, L, Estellés, V., & Moreno, J. (2007). Spectral calibration and atmospheric correction of ultra-fine spectral and spatial resolution remote sensing data. Application to CASI-1500 data. *Remote Sensing of Environment*, *109*(1), 54–65. Retrieved from http://www.scopus.com/inward/record.url?eid=2-s2.0-34248663498&partnerID=40&md5=8dbf718b13e09ead325cc348c29120d8

Guanter, L, Richter, R., & Kaufmann, H. (2009). On the application of the MODTRAN4 atmospheric radiative transfer code to optical remote sensing. *International Journal of Remote Sensing*, *30*(6), 1407–1424. Retrieved from http://www.scopus.com/inward/record.url?eid=2-s2.0-67650254778&partnerID=40&md5=812e62657ca35bdbed71bdd412864dd1

Guanter, Luis, Kaufmann, H., Segl, K., Foerster, S., Rogass, C., Chabrillat, S., … Sang, B. (2015). The EnMAP Spaceborne Imaging Spectroscopy Mission for Earth Observation. *Remote Sensing*, *7*(7), 8830–8857. doi:10.3390/rs70708830

Hank, T. B., Berger, K., Bach, H., Clevers, J. G. P. W., Gitelson, A., Zarco-Tejada, P., & Mauser, W. (2019, May 1). Spaceborne Imaging Spectroscopy for Sustainable Agriculture: Contributions and Challenges. *Surveys in Geophysics*. Springer Netherlands. doi:10.1007/s10712-018-9492-0

Helder, D., Thome, K. J., Mishra, N., Chander, G., Xiong, X., Angal, A., & Choi, T. (2013). Absolute radiometric calibration of landsat using a pseudo invariant calibration site. *IEEE Transactions on Geoscience and Remote Sensing*, *51*(3), 1360–1369. doi:10.1109/TGRS.2013.2243738

Lee, C. M., Cable, M. L., Hook, S. J., Green, R. O., Ustin, S. L., Mandl, D. J., & Middleton, E. M. (2015). An introduction to the NASA Hyperspectral InfraRed Imager (HyspIRI) mission and preparatory activities. *Remote Sensing of Environment*, *167*, 6–19. doi:10.1016/j.rse.2015.06.012

Loizzo, R., Guarini, R., Longo, F., Scopa, T., Formaro, R., Facchinetti, C., & Varacalli, G. (2018). Prisma: The Italian hyperspectral mission. In *International Geoscience and Remote Sensing Symposium (IGARSS)* (Vol. 2018-July, pp. 175–178). Institute of Electrical and Electronics Engineers Inc. doi:10.1109/IGARSS.2018.8518512

Matsunaga, T., Iwasaki, A., Tsuchida, S., Iwao, K., Tanii, J., Kashimura, O., … Tachikawa, T. (2018). Hisui status toward FY2019 launch. In *International Geoscience and Remote Sensing Symposium (IGARSS)* (Vol. 2018-July, pp. 160–163). Institute of Electrical and Electronics Engineers Inc. doi:10.1109/IGARSS.2018.8518639

Meroni, M., Busetto, L., Guanter, L., Cogliati, S., Crosta, G. F., Migliavacca, M., … Colombo, R. (2010). Characterization of fine resolution field spectrometers using solar Fraunhofer lines and atmospheric absorption features. *Applied optics*, *49*(15), 2858–2871. doi:10.1364/AO.49.002858

Middleton, E. M., Campbell, P. K. E., Ong, L., Landis, D. R., Zhang, Q., Neigh, C. S., … Pollack, N. H. (2017). Hyperion: The first global orbital spectrometer, earth observing-1 (EO-1) satellite (2000-2017). In *International Geoscience and Remote Sensing Symposium (IGARSS)* (Vol. 2017-July, pp. 3039–3042). Institute of Electrical and Electronics Engineers Inc.

doi:10.1109/IGARSS.2017.8127639

Müller, R., Avbelj, J., Carmona, E., Eckardt, A., Gerasch, B., Graham, L., … Walter, I. (2016). THE NEW HYPERSPECTRAL SENSOR DESIS ON THE MULTI-PAYLOAD PLATFORM MUSES INSTALLED ON THE ISS. *ISPRS - International Archives of the Photogrammetry, Remote Sensing and Spatial Information Sciences*, *XLI-B1*, 461–467. doi:10.5194/isprs-archives-XLI-B1-461-2016

Nieke, J., & Rast, M. (2018). Towards the copernicus hyperspectral imaging mission for the environment (CHIME). In *International Geoscience and Remote Sensing Symposium (IGARSS)* (Vol. 2018-July, pp. 157–159). Institute of Electrical and Electronics Engineers Inc. doi:10.1109/IGARSS.2018.8518384

Rascher, U., Alonso, L., Burkart, A., Cilia, C., Cogliati, S., Colombo, R., … Zemek, F. (2015). Sun-induced fluorescence - a new probe of photosynthesis: First maps from the imaging spectrometer *HyPlant*. *Global Change Biology*, *21*(12), 4673–4684. doi:10.1111/gcb.13017

Rast, M., & Painter, T. H. (2019, May 1). Earth Observation Imaging Spectroscopy for Terrestrial Systems: An Overview of Its History, Techniques, and Applications of Its Missions. *Surveys in Geophysics*. Springer Netherlands. doi:10.1007/s10712-019-09517-z

Richter, R., & Schläpfer, D. (2002). Geo-atmospheric processing of airborne imaging spectrometry data. Part 2: Atmospheric/topographic correction. *International Journal of Remote Sensing*, *23*(13), 2631–2649. doi:10.1080/01431160110115834

Roger, R. E., & Arnold, J. F. (1996). Reliably estimating the noise in AVIRIS hyperspectral images. *International Journal of Remote Sensing*, *17*(10), 1951–1962. doi:10.1080/01431169608948750

Scheffler, D., Hollstein, A., Diedrich, H., Segl, K., & Hostert, P. (2017). AROSICS: An Automated and Robust Open-Source Image Co-Registration Software for Multi-Sensor Satellite Data. *Remote Sensing*, *9*(7). doi:10.3390/rs9070676

Thompson, D. R., Babu, K. N., Braverman, A. J., Eastwood, M. L., Green, R. O., Hobbs, J. M., … Turmon, M. J. (2019). Optimal estimation of spectral surface reflectance in challenging atmospheres. *Remote Sensing of Environment*, *232*, 111258. doi:10.1016/J.RSE.2019.111258

Thompson, D. R., Boardman, J. W., Eastwood, M. L., Green, R. O., Haag, J. M., Mouroulis, P., & Van Gorp, B. (2018). Imaging spectrometer stray spectral response: In-flight characterization, correction, and validation. *Remote Sensing of Environment*, *204*, 850–860. doi:10.1016/J.RSE.2017.09.015

Thompson, D. R., Braverman, A., Brodrick, P. G., Candela, A., Carmon, N., Clark, R. N., … Wettergreen,

D. S. (2020a). Quantifying uncertainty for remote spectroscopy of surface composition. *Remote Sensing of Environment*, *247*, 111898. doi:https://doi.org/10.1016/j.rse.2020.111898

Thompson, D. R., Braverman, A., Brodrick, P. G., Candela, A., Carmon, N., Clark, R. N., … Wettergreen, D. S. (2020b). Quantifying uncertainty for remote spectroscopy of surface composition. *Remote Sensing of Environment*, *247*, 111898. doi:10.1016/j.rse.2020.111898

Thompson, D. R., Gao, B. C., Green, R. O., Roberts, D. A., Dennison, P. E., & Lundeen, S. R. (2015). Atmospheric correction for global mapping spectroscopy: ATREM advances for the HyspIRI preparatory campaign. *Remote Sensing of Environment*, *167*, 64–77. doi:10.1016/j.rse.2015.02.010

Thompson, D. R., Guanter, L., Berk, A., Gao, B. C., Richter, R., Schläpfer, D., & Thome, K. J. (2019, May 1). Retrieval of Atmospheric Parameters and Surface Reflectance from Visible and Shortwave Infrared Imaging Spectroscopy Data. *Surveys in Geophysics*. Springer Netherlands. doi:10.1007/s10712-018-9488-9

Thuillier, G., Hersé, M., Labs, D., Foujols, T., Peetermans, W., Gillotay, D., … Mandel, H. (2003). The solar spectral irradiance from 200 to 2400 nm as measured by the SOLSPEC spectrometer from the ATLAS and EURECA missions. *Solar Physics*, *214*(1), 1–22. doi:10.1023/A:1024048429145

Verhoef, W., & Bach, H. (2007). Coupled soil–leaf-canopy and atmosphere radiative transfer modeling to simulate hyperspectral multi-angular surface reflectance and {TOA} radiance data. *Remote Sensing of Environment*, *109*(2), 166–182. doi:http://dx.doi.org/10.1016/j.rse.2006.12.013

Verhoef, W., & Bach, H. (2012). Simulation of Sentinel-3 images by four-stream surface–atmosphere radiative transfer modeling in the optical and thermal domains. *Remote Sensing of Environment*, *120*, 197–207. doi:10.1016/j.rse.2011.10.034

Verhoef, W, Tol, C. Van Der, & Middleton, E. M. (2014). Vegetation Canopy Fluorescence and Reflectance Retrieval By Model Inversion Using Optimization. In *5th International Workshop on Remote Sensing of Vegetation Fluorescence* (pp. 759–770). Retrieved from http://congrexprojects.com/Custom/14C04/14C04_index.htm

Verhoef, Wouter, van der Tol, C., & Middleton, E. M. (2018). Hyperspectral radiative transfer modeling to explore the combined retrieval of biophysical parameters and canopy fluorescence from FLEX – Sentinel-3 tandem mission multi-sensor data. *Remote Sensing of Environment*, *204*, 942–963. doi:10.1016/j.rse.2017.08.006

Viallefont-Robinet, F., Helder, D., Fraisse, R., Newbury, A., van den Bergh, F., Lee, D., & Saunier, S.

(2018). Comparison of MTF measurements using edge method: towards reference data set. *Optics Express*, *26*(26), 33625. doi:10.1364/oe.26.033625